MalariAI: A Label-Resilient Decoupled Framework for Annotation-Agnostic Cell Segmentation and Explainable Stage Classification in Dense Malaria Blood Smears

Kaysarul Anas Apurba[a,*], Md Hasibul Hasan[b], Mohammed Ali[a], Tanzilur Rahman[a]

[a] *Department of Electrical and Computer Engineering, North South University, Dhaka 1229, Bangladesh*
[b] *Department of Computer Science and Engineering, International University of Business Agriculture and Technology (IUBAT), Dhaka 1230, Bangladesh*

arXiv:2607.00385v2 [eess.IV] 3 Aug 2026

Abstract

Automated malaria diagnosis from blood smear microscopy is a critical global health AI challenge; expert scarcity remains the primary diagnostic bottleneck. Existing deep learning systems face three compounding failures: end-to-end detectors treat unannotated cells as background, skewing recall by annotation completeness rather than true cell recovery; Non-Maximum Suppression suppresses valid detections in dense smears; and pipelines lack per-cell spatial evidence for clinical audit. We present MalariAI, a two-stage decoupled framework addressing all three. Stage 1 applies an annotation-agnostic watershed algorithm to isolate every cell in a full 1600×1200 image, recovering 75.95% of ground-truth cells without any ground-truth input. End-to-end, the pipeline reaches a binary parasitized AP@0.5 of 29.10% - the clinically relevant metric for flagging any infected cell - while the stricter multi-class mAP@0.5 of 8.67% mainly reflects watershed's organic region boundaries being penalized against axis-aligned ground-truth boxes, not a localisation failure. Stage 2 fine-tunes EfficientNet-B0 with Focal Loss on ground-truth crops, achieving 98.36% classification accuracy - an oracle upper bound once a cell is correctly localised - with 87.5% and 75.0% accuracy on the rare schizont and gametocyte stages, versus 38.45% and 57.27% AP for a modern YOLOv8s detector evaluated end-to-end on the same classes. Grad-CAM++ heatmaps generated per detected cell provide instance-level spatial evidence for clinical audit; a quantitative energy-in-box analysis confirms this activation is concentrated on the annotated cell body significantly above a geometric chance baseline (+0.0485, paired $p = 1.4 \times 10^{-33}$), letting microscopists verify predictions at the individual parasite level without sacrificing classification performance.

Keywords: Malaria detection, Blood smear analysis, Instance segmentation, Watershed algorithm, EfficientNet, Focal Loss, Explainable AI, Grad-CAM++, Medical image analysis, Decoupled framework

1. Introduction

Malaria remains one of the most consequential infectious diseases in contemporary global health. The World Health Organization reported 249 million cases worldwide in 2022, resulting in an estimated 608,000 deaths, of which 95% occurred in sub-Saharan Africa [1]. The burden falls disproportionately on children under five years of age and on populations with limited access to diagnostic infrastructure. Despite the existence of effective antimalarial therapies, a fundamental bottleneck persists at the point of diagnosis.

The clinical gold standard for malaria diagnosis is microscopic examination of a Giemsa-stained peripheral blood smear under a 100× oil-immersion objective. A trained microscopist inspects the slide, identifies red blood cells (RBCs) infected by *Plasmodium* parasites, and estimates the parasite stage from cellular morphology. The parasite lifecycle stage - ring, trophozoite, schizont, or gametocyte - carries direct implications for treatment selection and disease severity assessment [2]. This manual process requires 20–30 minutes per slide, specialized training that takes years to acquire, and physical equipment that is not universally available in endemic regions. The result is a diagnostic bottleneck that costs lives.

The promise of deep learning for automated malaria diagnosis has generated substantial research interest over the past decade [3]. Convolutional neural networks (CNNs) have demonstrated strong performance on cell-patch classification tasks [4, 5], and end-to-end object detectors such as Faster R-CNN [6] and YOLO [7] have been applied to the whole-slide detection problem. However, no single published system has achieved the combination of properties required for genuine clinical deployment: annotation resilience, dense-region recall, multi-class stage classification, and integrated spatial explainability.

Our analysis of the existing literature identifies three specific, measurable failure modes that collectively prevent any current system from being clinically deployable:

*Corresponding author.
Email address: kaysarulanas2@gmail.com (Kaysarul Anas Apurba)
URL: tanzilur.rahman@northsouth.edu (Tanzilur Rahman)

P1: Incomplete Annotation. The NIH BBBC041 benchmark - the de facto standard for malaria detection research - annotates only infected cells and a subset of healthy RBCs. End-to-end detectors trained on this data learn to treat unannotated cells as background, producing false positives on any cell the annotators happened to skip. Validation loss in such systems plateaus early and subsequently *increases*, a pattern our Baseline A experiments confirm and diagnose as a structural consequence of label incompleteness rather than model overfitting.

P2: Dense Overlap and NMS Failure. Our exploratory analysis of BBBC041 finds that 58% of training images contain at least one ground-truth pair with IoU > 0.3, with a maximum of 223 annotated cells per image. All anchor-based detectors apply Non-Maximum Suppression (NMS) to filter proposals, but NMS assumes overlapping proposals are duplicates of the same object. In dense smear regions, this assumption fails, causing systematic deletion of true positive detections.

P3: Black-Box Output. While image-level explainability methods such as Grad-CAM and SHAP have been applied to malaria image classification [8, 9, 10], these approaches highlight broad regions within a whole image rather than individual parasite instances. No published whole-slide *detection* pipeline produces per-cell spatial evidence that clinicians could use to validate, audit, or override predictions at the instance level - the granularity required for meaningful clinical audit trails [11, 12].

These failure modes are not historical artefacts of early deep learning research. A survey of published systems from 2024–2026 confirms that all three remain unresolved: state-of-the-art classification approaches based on EfficientNet, ConvNeXt, and hybrid CNN architectures achieve high accuracy on pre-cropped, individually segmented cell patches with binary labels [13, 14, 15, 16], but no recent system operates on whole blood smear images, resolves annotation-incomplete training, or provides per-cell spatial explainability on the full slide. Concurrently, Issah *et al.* [17] demonstrate that the latest YOLO-based whole-slide detectors still suffer performance drops exceeding 80% under cross-dataset evaluation, confirming that annotation sensitivity (P1) and generalisation failure remain active barriers to clinical deployment. This conclusion is consistent with the recent systematic review by Sukumarran *et al.* [18], which identifies binary classification, weak cross-dataset validation, and limited multi-stage/species classification as persistent gaps in automated malaria diagnosis from microscopic blood smears.

We present MalariAI, a two-stage decoupled framework designed to address all three failure modes. The key insight is that cell *localisation* and cell *classification* are biologically distinct sub-problems that benefit from different inductive biases. By separating them into sequential, independently optimized stages, MalariAI avoids the annotation dependency of end-to-end detection (P1), bypasses the NMS step (P2), and enables per-cell spatial explainability to be applied after classification (P3).

This paper makes four concrete contributions:

C1. Label-Resilient Cell Segmentation (C1). An annotation-agnostic Stage 1 based on distance-transform guided watershed recovers 75.95% of ground-truth cells by centroid localisation (66.88% at strict IoU $\geq$ 0.5) on the 120-image BBBC041 test set *without consulting any annotation*, structurally eliminating Problem P1 from the pipeline.

C2. Density-Invariant Instance Separation (C2). Distance-transform watershed operates at the morphological level and does not apply NMS. Touching cells in dense smear regions are separated at the instance level by the distance-transform topology, bypassing Problem P2.

C3. Integrated End-to-End Spatial Explainability (C3). Grad-CAM++ heatmaps are generated for every cell detected in a full blood smear image, producing a two-view output: a 160-pixel crop overlay and a full-image heatmap localising all parasite activations simultaneously. To our knowledge, this is the first whole-slide malaria detection system to integrate per-cell spatial explainability as a first-class output.

C4. Cross-Dataset Generalisation Assessment (C4). The complete pipeline is evaluated zero-shot on MP-IDB (209 images, 17 patients, four *Plasmodium* species) without any hyperparameter re-tuning, providing an honest out-of-distribution characterisation that is rare in the malaria detection literature and directly quantifies the gap between source-domain performance and real-world deployment conditions.

Individually, distance-transform watershed, EfficientNet-B0, Focal Loss, and Grad-CAM++ are each established techniques; the engineering contribution of MalariAI is their decoupled integration (C1–C3). Separately, and on its own footing, Section 4.2.2 introduces four complementary localisation metrics (M1–M4) that disentangle true missed detections from boundary mis-alignment artefacts specific to organic-shaped segmentation - a measurement contribution applicable to any watershed-based or otherwise non-rectangular detector evaluated against box-based ground truth, not just to MalariAI itself.

Table 1 positions MalariAI against the most closely related prior systems across the three failure modes above; no prior system resolves all three jointly.

Paper organisation. Section 2 reviews the related literature across five thematic areas. Section 3 describes the

Table 1: Positioning of MalariAI against prior work. **P1** = annotation-agnostic detection; **P2** = dense overlap handling without NMS; **P3** = integrated per-cell spatial XAI on whole-slide images. ✓ = addressed; ∼ = partial; × = not addressed.

System	P1	P2	P3
Singh *et al.* [5]	×	×	×
Loh *et al.* [19]	×	×	×
Optimized YOLOv4 [7]	×	×	×
Delgado-Ortet *et al.* [20]	×	×	×
Pandiaraj *et al.* [21]	×	∼	×
XAI ensemble [10]	×	×	∼
CellSAM [22]	×	✓	×
Disco [23]	×	✓	×
MalariAI (ours)	✓	✓	✓

dataset, system overview, and evaluation metrics. Section 4 presents quantitative and qualitative results, including a zero-shot cross-dataset evaluation on the held-out MP-IDB benchmark. Section 5 discusses implications and limitations. Section 6 concludes with directions for future work.

2. Related Work

We organize the literature into five thematic areas: (i) classical and feature-based approaches, (ii) CNN-based classification on pre-isolated cells, (iii) end-to-end object detection and instance segmentation, (iv) two-stage decoupled pipelines, and (v) explainable AI for clinical malaria diagnosis. We conclude with a cross-cutting analysis of open problems.

2.1. Classical and Feature-Based Approaches

Early automated malaria diagnosis relied on carefully engineered image processing pipelines applied to Giemsa- or May–Grünwald–Giemsa (MGG)-stained blood smears. The dominant approach combined global thresholding (*e.g.*, Otsu's method [24]), morphological operations such as erosion and dilation, and hand-crafted feature descriptors (*e.g.*, shape moments, color histograms, Gabor texture features) fed into classical classifiers such as Support Vector Machines (SVM) or Random Forests [3].

These pipelines established a fundamental insight that malaria detection is a two-phase problem: cells must first be localized before their internal morphology can be assessed. However, they suffered from two compounding weaknesses. Segmentation quality degraded sharply when cells overlapped, and hand-crafted features failed to generalize across staining protocols, microscope configurations, and acquisition sites [3, 20]. Nonetheless, classical watershed segmentation based on the distance transform [25] remains competitive for the cell *localisation* sub-problem: it requires no labeled training data, its convergence is deterministic, and it is naturally suited to the circular morphology of red blood cells. This motivates our adoption of distance-transform watershed as Stage 1.

Most closely related to our Stage 1 design, Angkoso *et al.* [26] benchmark five classical segmentation techniques – Watershed, Fuzzy C-Means, K-means, Gaussian Mixture Models, and Entropy Filtering – within a color-cascading preprocessing framework (RGB normalization, gamma correction, noise reduction, exposure compensation, edge enhancement) on 574 microscopy images spanning four *Plasmodium* species. Fuzzy C-Means is reported as the most reliable method overall (98.26% accuracy, 97.91% sensitivity, 98.61% specificity), with Watershed competitive on well-contrasted images but comparatively less consistent on faint or overlapping structures. This result is complementary rather than overlapping with our contribution: Angkoso *et al.* evaluate segmentation quality as a pixel-wise classification task (parasite vs. non-parasite pixels) on a private clinical dataset, with no cell-level detection output, no species or lifecycle-stage classification, and no deep learning component – their own stated future work explicitly identifies integrating a deep learning architecture such as U-Net and adding stage classification as open directions. MalariAI addresses precisely this gap: Stage 1's watershed output is annotation-free cell-level *detection* (bounding boxes, not pixel masks) feeding a downstream 7-class deep learning classifier (Stage 2), validated on public benchmarks (BBBC041, MP-IDB) with cross-dataset generalisation and per-cell explainability, none of which Angkoso *et al.* address. The two studies are best read as adjacent: Angkoso *et al.* establish that Watershed is a reasonable but not uniquely dominant classical segmentation choice among non-learned alternatives, which is consistent with our own decision (Section 4.2.3) to benchmark Stage 1's watershed against a learned alternative rather than assume its superiority.

2.2. CNN-Based Classification of Pre-Isolated Cells

The release of the NIH malaria cell image dataset [4], comprising individually cropped and labeled cell patches, catalyzed CNN classification studies. Rajaraman *et al.* [4] evaluated fine-tuned architectures (VGG-16, ResNet-50, Xception) and found that transfer learning from natural image corpora substantially outperformed training from scratch.

More recently, Singh *et al.* [5] propose an optimized hybrid framework combining a 12-layer CNN with EfficientNet-B7 through a parallel feature-fusion head. Otsu-based preprocessing of the RGB images enhances parasite-relevant regions before classification, yielding 97.96% accuracy on their 43,400-image dataset. Segmentation quality on a manually annotated 100-image subset achieves a Dice coefficient of 0.848 and Jaccard Index of 0.738. The approach is conceptually related to our Stage 2 design, but it operates exclusively on pre-cropped, individually isolated cell patches. The cell isolation problem - finding cells in a dense, unannotated whole slide - is absent. The authors explicitly acknowledge that "interpretability tools need to

be refined to become clinically applicable" and identify real-time deployment as future work [5].

This family of work collectively avoids the hard subproblem of whole-slide cell detection. Reported accuracy metrics measure only classification on pre-isolated patches and cannot be compared to detection system benchmarks.

2.3. End-to-End Object Detection and Instance Segmentation

The Faster R-CNN architecture [6] - combining a Region Proposal Network (RPN) with a two-stage classification head over a ResNet-50 [27] Feature Pyramid Network (FPN) [28] backbone - was among the first deep learning systems applied directly to the whole-slide malaria detection problem. Hung *et al.* [29] demonstrated high accuracy using a cascaded Faster R-CNN with an AlexNet backbone, establishing the feasibility of end-to-end detection. Subsequent work has explored lighter architectures: optimized YOLOv4 models with backbone replacement and layer pruning achieve strong mAP on thin smear images [7]. Rather than only citing this trajectory toward faster single-stage detectors, Section 3.4 additionally trains and evaluates YOLOv8s [30] directly on our data as Baseline B, alongside Faster R-CNN Baseline A.

Instance segmentation - producing a pixel-level mask per detected cell - was explored by Loh *et al.* [19] using Mask R-CNN [31]. Their model achieves inference speeds 15× faster than manual counting. These results represent the closest prior art to our Baseline A evaluation. Transformer detectors provide a complementary NMS-free direction: DN-DETR [32] accelerates DETR training by denoising ground-truth queries while retaining set-based prediction and Hungarian matching. However, such detectors still require complete bounding-box supervision during training. In a sparsely annotated smear dataset, the closed-world label problem therefore remains even if NMS is removed. In malaria specifically, Guemas *et al.* [33] evaluate a real-time detection transformer (RT-DETR) for patient-level recognition of four *Plasmodium* species from thin blood smears, using a large manually labelled corpus across multiple hospitals. This work confirms that transformer-style detectors are entering malaria microscopy, but its focus is species recognition from labelled thin-smear data rather than annotation-agnostic universal cell recovery, dense-cell instance separation, or per-cell spatial explainability.

However, end-to-end detectors exhibit two systematic failure modes in the malaria domain. First, all such models operate under the closed-world assumption: any region without a ground-truth bounding box is treated as background during training. In NIH BBBC041, annotation is incomplete; a detector trained on this data suppresses unannotated cells, producing recall figures that reflect annotation density rather than true cell recovery rate. Loh *et al.* [19] acknowledge this, proposing semi-automated labeling to reduce annotation bias. This limitation remains an active concern: Issah *et al.* [17] demonstrate that state-of-the-art YOLOv12 architectures trained on curated malaria datasets suffer performance drops exceeding 80% under cross-dataset evaluation, confirming that end-to-end detectors remain sensitive to the annotation characteristics of their training sets when deployed in new settings. The annotation incompleteness problem (P1) is not confined to the malaria domain: Bai *et al.* [34] document that the widely-used DeepLesion benchmark has a missing annotation rate of approximately 50%, and demonstrate that training end-to-end detectors directly on such data yields suboptimal recall [34]. Their ET-ULD framework addresses this through iterative pseudo-label mining, but still requires a reliably annotated initial subset. MalariAI's annotation-agnostic watershed requires no labeled data at the detection stage, structurally eliminating this dependency.

Second, Non-Maximum Suppression (NMS) calibrated for non-overlapping objects fails in dense smear regions where genuine cells share high IoU. Rather than solving this, prior work filters out dense images before evaluation [19], sacrificing exactly the images where automated diagnosis is most needed. This failure mode has been independently confirmed at the highest-impact venues: Marks *et al.* [22] explicitly state that R-CNN-family detectors "rely on non-maximum suppression (NMS), leading to missed instances in crowded scenes with irregular morphologies or high degrees of overlap" and present CellSAM – a SAM-based segmentation framework built on the promptable Segment Anything foundation model [35] – as a workaround requiring pixel-level mask annotations that are unavailable in the malaria setting. Formally, Sun *et al.* [23] conduct the first systematic analysis of cell adjacency graph topology across four histopathology benchmarks, demonstrating that real-world cellular arrangements are fundamentally non-bipartite – characterized by odd-length cycles that make NMS-based instance disambiguation inherently infeasible. Their measured conflict-node ratio reaches 30.49% in the GBC-FS 2025 gallbladder dataset, providing a rigorous graph-theoretic foundation for our empirical finding that 58% of BBBC041 images contain ground-truth cell pairs with IoU > 0.3.

2.4. Two-Stage Decoupled Pipelines

The closest architectural precedents to MalariAI separate cell segmentation from cell classification into sequential stages. Encoder-decoder architectures — pioneered by U-Net [36] for biomedical image segmentation and extended by SegNet [37] and UNet++ [38] — provide the segmentation backbone underpinning most such pipelines. Rather than adopt one of these supervised segmentation networks as Stage 1, MalariAI instead uses an annotation-free watershed algorithm; Section 4.2.3 reports a direct, same-test-set quantitative comparison against a trained U-Net baseline to characterize this design choice empirically rather than by assumption. More recently, CellViT [39] demonstrates that Vision Transformer encoders can jointly address cell segmentation and classification in histopathology, though at

substantially higher computational cost than a decoupled approach.

Delgado-Ortet *et al.* [20] present a three-stage pipeline comprising a SegNet [37]-based encoder-decoder segmentation network, a crop-and-mask stage, and a 13-layer CNN classifier, achieving 93.72% global segmentation accuracy and 87.04% malaria detection specificity on MGG-stained smears. The work demonstrates decoupled pipeline viability but suffers from three failures: the segmentation network misclassifies leukocytes and platelets, inducing cascading classification errors; the classifier overfits from 95.0% validation to 75.39% test accuracy due to a five-patient training set; and class imbalance is unaddressed. Their stated future directions encompass annotating additional cell classes, generating larger datasets, and mixing data across institutions; taken together, these align closely with the improvements MalariAI implements.

More recently, **Pandiaraj *et al.*** [21] combine a TransMobileUNet++ segmentation network with an Adaptive and Atrous Convolution-based Recurrent MobileNetV2 detection backbone, reporting 94.88% accuracy on Kaggle-hosted pre-cropped cell image datasets. However, the framework performs binary classification only (parasitized vs. uninfected), does not operate on whole blood smear images, and reports no mAP metric at any IoU threshold, precluding quantitative comparison with standardized detection benchmarks. Furthermore, their metaheuristic optimization introduces severe reproducibility concerns: sensitivity to random initialization and the absence of convergence guarantees makes independent replication impractical [21].

Consequently, while the two-stage literature suggests that architectural decoupling is the correct design direction, no existing system jointly addresses annotation resilience, dense-region recall, multi-class imbalance, and spatial explainability.

2.5. Explainable AI for Clinical Malaria Diagnosis

Physician trust in AI systems depends on the availability of spatial evidence for model predictions [10]. Gradient-weighted Class Activation Mapping (Grad-CAM) [11] and its extension Grad-CAM++ [12] produce spatial heatmaps by weighting convolutional feature maps by class-specific gradient signals. In the malaria context, these maps should ideally localize the parasite body within the infected cell.

Several recent works demonstrate meaningful Grad-CAM outputs on malaria cell images. Transformer-based models with compact convolutional heads produce interpretable attention maps for parasite detection [9]. Ensemble frameworks with XAI integration have been benchmarked against clinical diagnostic criteria [10]. However, *all* existing XAI applications in the malaria literature operate on pre-cropped single-cell patches. No published system integrates spatial explainability into a pipeline that performs whole-slide detection, cell segmentation, classification, and explanation end-to-end. MalariAI closes this gap: Grad-CAM++ is applied within the Stage 2 classifier to crops produced by Stage 1, making every cell in a full blood smear image explainable without requiring pre-isolation. Detection-specific XAI methods such as D-RISE [40] show that object-detector predictions can be explained with saliency maps, but their black-box masking strategy requires many perturbed forward passes per target detection. This makes them useful for detector auditing but less suited to routine whole-slide malaria screening, where dozens or hundreds of cell instances may require explanation in a single smear. The broader importance of whole-slide spatial analysis over patch-level processing is affirmed by recent computational pathology infrastructure: Zheng *et al.* [41] introduce LazySlide (Nature Methods, 2026), identifying fragmented patch-based workflows as a primary barrier to clinical adoption in digital pathology, and establishing whole-slide cell segmentation and zero-shot classification as the target capability. MalariAI achieves this in the malaria domain through its integrated detection, classification, and Grad-CAM++ pipeline on full 1600×1200 blood smear images.

2.6. Cross-Cutting Open Problems and Positioning

Table 1 (Section 1) summarizes how the most closely related prior works address the three open problems. In addition, the cross-dataset setting addressed in Contribution C4 is a known barrier across medical image analysis: Guan and Liu [42] survey domain adaptation methods and identify domain shift between source and target medical image distributions as a central obstacle to robust deployment. This directly contextualizes our zero-shot BBBC041-to-MP-IDB experiment: MalariAI does not claim domain adaptation is solved, but explicitly measures the shift and exposes where Stage 1 requires dataset-adaptive parameters. Recent malaria dataset releases reinforce the importance of this direction: Nakasi *et al.* [43] publish a Uganda mobile-microscopy benchmark containing annotated thick and thin blood smear images, while also noting thin-smear limitations in species and life-cycle diversity. Such datasets are natural future test beds for MalariAI's cross-dataset evaluation, but they do not remove the need to report source-to-target performance honestly.

3. System Overview and Methodology

3.1. Dataset Description

3.1.1. Primary Dataset: BBBC041

Dataset.. All experiments use the NIH BBBC041 benchmark [44], a publicly available collection of Giemsa-stained thin *Plasmodium falciparum* blood smear images acquired at 100× oil-immersion magnification. The dataset comprises 1,208 training images and 120 held-out test images, each at 1,600 × 1,200 pixels (RGB). Raw annotations total 80,113 bounding boxes in training and 5,922 in testing across seven categories. Following standard practice, *difficult* annotations (441 training; 5 test) are excluded from all evaluations, yielding 79,672 and 5,917 valid boxes respectively.

Class distribution and imbalance.. Table 2 and Figure 1 report per-class annotation counts. The distribution is severely imbalanced: red blood cells constitute 97.2% of training annotations, while gametocytes account for only 0.18% - a ratio of 537:1. A model predicting *red blood cell* for every instance achieves 97.2% accuracy while detecting zero parasites. This motivates Focal Loss [45] with per-class inverse frequency weights in Stage 2 (Section 3.2.3).

Table 2: Per-class annotation counts in NIH BBBC041 (*difficult* annotations excluded).

Class	Train	Test	% of Train
Red blood cell	77,420	5,614	97.18%
Trophozoite	1,473	111	1.85%
Ring	353	169	0.44%
Schizont	179	11	0.22%
Gametocyte	144	12	0.18%
Leukocyte	103	0	0.13%
Total	79,672	5,917	

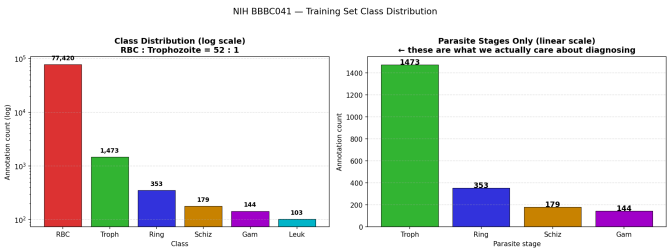


Figure 1: Class distribution of NIH BBBC041 training annotations. Left: log-scale view dominated by the red blood cell class (77,420 instances). Right: linear-scale view of parasitic stages only, showing the secondary imbalance between trophozoites (1,473) and the rarest stages (gametocyte: 144). The 537:1 RBC-to-gametocyte ratio motivates per-class Focal Loss weighting.

Parasitic stage morphology.. Figure 2 shows representative crops for each parasitic stage. Ring-stage infections present as pale discs with only a faint peripheral chromatin outline, closely resembling uninfected RBCs. Trophozoites exhibit irregular chromatin mass; schizonts show clear internal segmentation (merozoites); gametocytes appear as large, densely stained elongated bodies. This morphological hierarchy directly predicts which classes the Stage 2 classifier will find most challenging.

Annotation density and cell overlap.. Figure 3 shows the distribution of annotated boxes per image. Density ranges from 9 to 223 boxes, with a median of 59 and a 95th percentile of 137; 11% of images exceed 100 cells. To quantify Problem P2, we computed pairwise IoU between all ground-truth boxes within each image over a 200-image sample. **58%** of images contain at least one ground-truth pair with IoU > 0.3, confirming that cell overlap is a structural feature of the data. This empirical finding directly motivates distance-transform watershed as Stage 1.

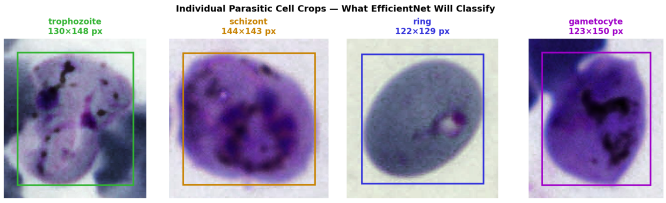


Figure 2: Representative ground-truth crops of each parasitic stage in NIH BBBC041 at native resolution. Ring-stage infections are visually the most similar to healthy RBCs, predicting lower per-class accuracy for that class. Parasitic stages are systematically larger than healthy erythrocytes (trophozoite median area: 17,272 px^2; RBC: 11,544 px^2), consistent with intraerythrocytic swelling during parasite development.

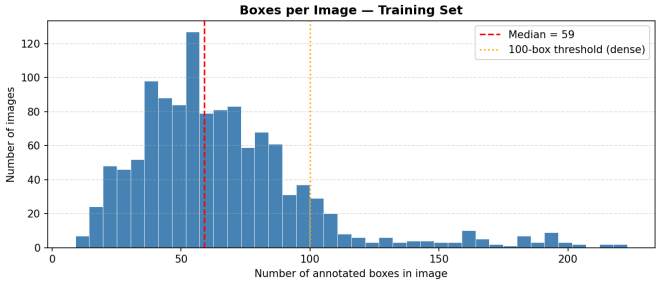


Figure 3: Distribution of annotated bounding boxes per image in the BBBC041 training set (1,208 images). The dashed red line marks the median (59 boxes); the dotted orange line at 100 boxes identifies images we classify as *dense smears*. 11% of images exceed this threshold. 58% of a 200-image sample contain at least one overlapping cell pair (IoU > 0.3), confirming the severity of the NMS failure mode.

Train/validation/test protocol.. The 1,208 training images are partitioned 80/20 at the image level into training (966 images) and validation (242 images) splits. No image contributes boxes to both sets. The random seed is fixed at 42 for reproducibility. All hyperparameter decisions use the validation split exclusively. The 120 test images are held out for Stage 1 evaluation only.

3.1.2. Cross-Dataset Validation: MP-IDB

To assess generalisation beyond the NIH BBBC041 benchmark, we adopt the *Malaria Parasite Image Database* (MP-IDB) [46] as a held-out cross-dataset evaluation set. MP-IDB comprises 209 images from 17 distinct patient samples, acquired at 2,592×1,944 pixels under Giemsa thin-smear staining - the same staining protocol as BBBC041, but a different institution, magnification calibration, and patient cohort. Annotations were released in Supervisely bitmap-mask format; we decode each mask via base64 → zlib → PNG and derive tight bounding boxes from the mask origin and dimensions, yielding 1,407 annotated infected cells (script: `data/prepare_mpidb.py`).

Taxonomy mismatch.. MP-IDB labels cells at the *species* level (*P. falciparum*, *P. vivax*, *P. malariae*, *P. ovale*), whereas BBBC041 labels cells at the *lifecycle stage* level (ring, trophozoite, schizont, gametocyte). These taxonomies are orthogonal: species identity does not determine lifecycle stage. Accordingly, MP-IDB evaluation is *binary*: any annotated object is an infected cell (positive), and the pipeline's task is to detect it regardless of species or stage.

Species and stage distribution.. Figure 4 shows the species breakdown. *P. falciparum* dominates (1,267 cells, 90.0%), reflecting its prevalence in clinical thin-smear datasets globally. Figure 5 reports image-level lifecycle stage tags (multi-label): ring stage appears in 125 images (60%), trophozoite in 54 (26%), schizont in 38 (18%), and gametocyte in 26 (12%), providing cross-stage diversity despite the species-only annotation granularity.

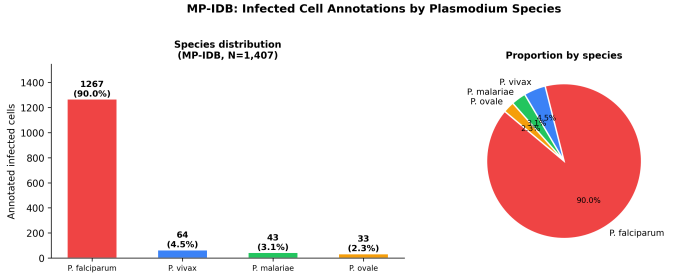


Figure 4: MP-IDB species distribution. Left: annotation counts per *Plasmodium* species across 209 images. *P. falciparum* comprises 90.0% of all annotated infected cells (1,267 of 1,407), consistent with its epidemiological prevalence. Right: proportional breakdown. The severe species imbalance mirrors the stage imbalance in BBBC041 and motivates binary (infected vs. uninfected) cross-dataset evaluation.

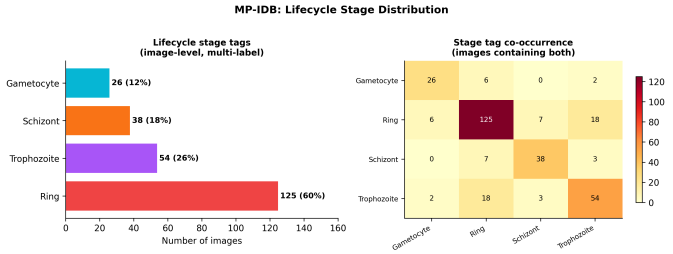


Figure 5: MP-IDB lifecycle stage distribution. Left: number of images containing each stage tag (multi-label; one image may carry multiple tags). Ring-stage infections are the most common (60% of images). Right: tag co-occurrence matrix - the 18 images tagged with both ring and trophozoite indicate mixed-stage smears, reflecting real clinical variability. Stage tags are image-level only; individual infected cells are not labeled by stage.

Resolution and scale gap.. A critical difference from BBBC041 is the bounding-box area of infected cells. Figure 6 shows that the median infected-cell area in MP-IDB is 3,933 px^2, compared with 16,875 px^2 for parasitic-stage cells in BBBC041 - a 4.3× reduction in absolute size. This is not a biological difference: cells are the same physical size in both datasets. Rather, it reflects a difference in pixel density per cell: MP-IDB images contain 2.63× more pixels overall (5.04 Mpx vs. 1.92 Mpx) but fewer magnification-normalized pixels per cell, so each infected cell covers only 0.078% of the image frame versus 0.879% in BBBC041 - an 11.3× reduction in relative prominence. Figure 7 illustrates this geometrically.

This scale gap has a direct consequence for Stage 1: the watershed hyperparameters `MIN_DIST` = 12 px and `MIN_AREA` = 150 px^2 were tuned on BBBC041. For MP-IDB, the resolution-corrected `MIN_DIST` is approximately 20 px, and the characteristic infected-cell radius is only 35 px versus 73 px in BBBC041. Cross-dataset evaluation on MP-IDB therefore provides an *honest* assessment of the pipeline's out-of-distribution behavior without any parameter re-tuning, and simultaneously motivates the Stage 1 adaptive improvements described in future work (Section 5.3).

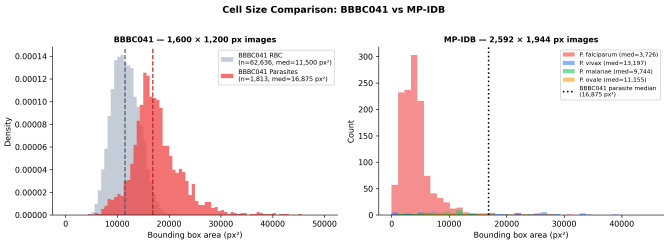


Figure 6: Bounding-box area distributions for BBBC041 (left) and MP-IDB (right). Left: BBBC041 RBC and parasite distributions overlap substantially; the parasite median (16,875 px^2) lies well above the RBC median (11,500 px^2), reflecting intraerythrocytic swelling during parasite development. Right: MP-IDB infected-cell areas cluster at far lower values (median 3,933 px^2 for *P. falciparum*), 4.3× smaller than the BBBC041 parasite median (dotted line). *P. vivax* and *P. ovale* show larger median areas (13,197 and 11,155 px^2 respectively), consistent with their known tendency to infect larger reticulocytes. This scale gap is expected to reduce Stage 1 recall on MP-IDB when applied without parameter re-tuning.

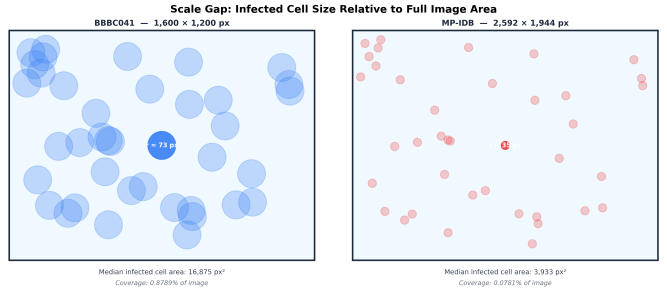


Figure 7: Geometric illustration of the scale gap between BBBC041 (left) and MP-IDB (right). Each circle represents an infected cell drawn to scale relative to the image frame. In BBBC041 the highlighted cell (radius $r \approx 73$ px) covers 0.88% of the image; in MP-IDB the corresponding cell (radius $r \approx 35$ px) covers only 0.078%. Watershed parameters tuned on BBBC041 underperform on MP-IDB without resolution-aware adaptation.

Table 3 summarizes the key properties of both datasets side by side.

Table 3: Comparison of primary (BBBC041) and cross-validation (MP-IDB) datasets.

Property	**BBBC041 (primary)**	**MP-IDB (cross-val)**
Source	NIH / Broad Institute	Delgado-Ortet et al. (2020)
Images	1,328 (train + test)	209 (annotated)
Resolution	1,600×1,200 px	2,592×1,944 px
Annotation type	Bounding boxes	Bitmap masks → boxes
Label taxonomy	Stage-level	Species-level
Infected cells	1,841	1,407
Median cell area	16,875 px^2	3,933 px^2
Cell image coverage	0.879%	0.078%
Patients	Not reported	17
Staining	Giemsa thin smear	Giemsa thin smear

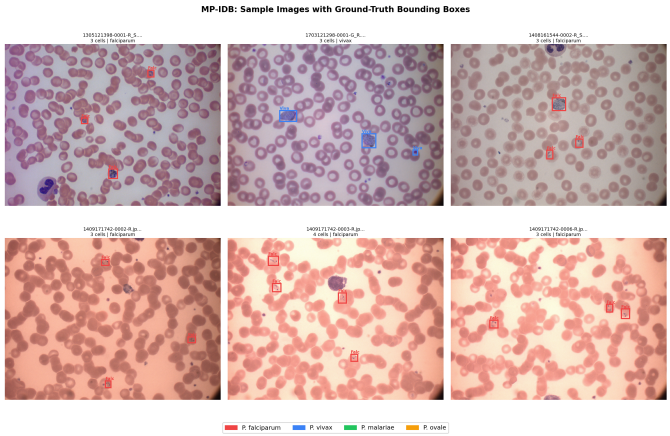


Figure 8: Representative MP-IDB images with ground-truth bounding boxes overlaid. Red boxes: *P. falciparum*; blue: *P. vivax*; green: *P. malariae*; yellow: *P. ovale*. Images span multiple patients and lifecycle stages. The top row shows standard Giemsa staining; the bottom row shows images from a patient with slightly different background coloration, illustrating intra-cohort staining variability. Infected cells are visually subtle relative to the large number of healthy RBCs, confirming the detection challenge.

3.2. Proposed MalariAI Framework

3.2.1. Overall Pipeline Architecture

MalariAI follows a two-stage decoupled design, illustrated in Figure 9. Stage 1 operates directly on the raw blood smear image and produces a set of candidate cell bounding boxes using an annotation-agnostic watershed algorithm – no ground-truth labels are consulted at any point. Stage 2 receives each cropped cell region and classifies it independently using a focal-loss-trained EfficientNet-B0 classifier. A Grad-CAM++ module then attaches a spatial heatmap to every detected cell, enabling per-cell visual audit trails. This decoupling deliberately separates the segmentation problem (dense, overlapping cells in a high-resolution slide) from the classification problem (fine-grained morphological discrimination within a single-cell crop), allowing each stage to be optimised and evaluated independently.

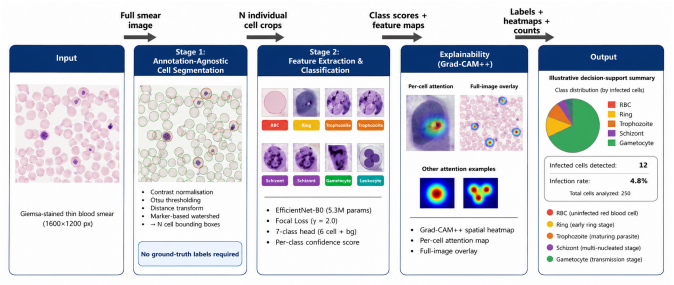


Figure 9: MalariAI two-stage decoupled architecture. Stage 1 performs universal cell segmentation via distance-transform guided watershed on the raw 1600×1200 blood smear image with no annotation input. Stage 2 classifies each 64×64 crop with EfficientNet-B0 and Focal Loss, followed by Grad-CAM++ for per-cell spatial explainability.

3.2.2. Stage 1 – Annotation-Agnostic Cell Segmentation

Stage 1 applies a five-step computer vision pipeline to produce an ordered set of bounding boxes $\mathcal{B} = \{(x_1^i, y_1^i, x_2^i, y_2^i)\}_{i=1}^{N}$ from a raw blood smear image $\mathbf{I} \in \mathbb{R}^{H\times W\times 3}$, where N is determined entirely by the image content and no ground-truth annotation is consulted at any step.

Step 1: Grayscale conversion and Otsu thresholding.. The input BGR image is converted to a single-channel grayscale image $G \in \mathbb{R}^{H\times W}$ using the standard luminosity transform. Otsu's method [24] selects the threshold τ^* that maximizes inter-class variance between foreground (cells) and background:

$$\tau^* = \arg\max_{\tau}\ \omega_0(\tau)\,\omega_1(\tau)\left[\mu_0(\tau) - \mu_1(\tau)\right]^2 \qquad (1)$$

where ω_k and μ_k are the prior probability and mean gray level of class k. The binary mask is formed as $B = \mathbf{1}[G < \tau^*]$ (inverse: cells are dark, background is bright in Giemsa-stained smears), so foreground pixels take value 255 and background pixels take 0.

Step 2: Morphological opening.. A morphological opening with a 3×3 elliptical structuring element applied for two

iterations removes thin noise filaments from the binary mask while preserving cell bodies:

$$O = (B \ominus K) \oplus K \tag{2}$$

where $\ominus$ denotes erosion and $\oplus$ denotes dilation. The small kernel size (3 px) is chosen to minimize erosion of cell boundaries, which is important for accurately locating watershed seeds at cell centers.

Step 3: Euclidean distance transform.. The Euclidean distance transform D assigns to each foreground pixel (x, y) its minimum distance to any background pixel:

$$D(x, y) = \min_{(p,q) \notin O} \sqrt{(x-p)^2 + (y-q)^2} \tag{3}$$

Peaks in D correspond to cell centers: a pixel at the center of a perfectly circular cell of radius r achieves $D = r$, while pixels near the boundary achieve $D \approx 0$. In dense regions, the distance transform naturally produces a ridge between adjacent cells, creating the topological separator that watershed uses for instance-level splitting.

Step 4: Seed extraction via local maxima.. Seeds for the watershed algorithm are extracted as local maxima of D that satisfy two conditions: (i) they are separated by at least `MIN_DIST` = 12 pixels from any higher-valued maximum, and (ii) they exceed an absolute threshold $\tau_{\text{seed}} = 0.25 \times D_{\max}$. The minimum distance of 12 px (compared to the typical RBC radius of ∼50 px) ensures one seed per cell without suppressing seeds in adjacent cells. The distance threshold of 0.25 places seeds only at genuine cell centers, not at shallow bumps caused by staining artefacts.

Step 5: Watershed segmentation and bounding box extraction.. Seeds are labeled as independent markers and watershed is applied to the negated distance map $-D$ with the binary mask O as the allowed domain:

$$\mathcal{L} = \text{watershed}(-D,\ \text{markers},\ \text{mask} = O) \tag{4}$$

Each labeled region ℓ in $\mathcal{L}$ yields a bounding box (x_1, y_1, x_2, y_2) from the extreme pixel coordinates of that region. Regions with fewer than `MIN_AREA` = 150 pixels are discarded as noise. A compactness parameter of 0.1 regularises elongated regions produced by connected cell clusters, biasing watershed boundaries toward the topological saddle points in D.

Figure 10 summarizes the complete Stage 1 procedure.

Algorithm 1: Stage 1 – Annotation-Agnostic Watershed
Require: Image $\mathbf{I} \in \mathbb{R}^{H \times W \times 3}$
Ensure: Boxes $\mathcal{B} = \{(x_1^i, y_1^i, x_2^i, y_2^i)\}$

```
G ← BGR2GRAY(I)
τ* ← OtsuThreshold(G)
B ← 1[G < τ*]    // cells
O ← MorphOpen(B, k=3, iters=2)
D ← DistanceTransform(O)
S ← LocalMaxima(D,
      d_min=12, τ_seed=0.25 D_max)
M ← LabelSeeds(S)
L ← watershed(−D, M, O); B ← ∅
for each ℓ ∈ L:
    if |ℓ| ≥ 150 then B ← B ∪ {BBox(ℓ)}
return B
```

Figure 10: Stage 1 annotation-agnostic watershed segmentation (Algorithm 1). Parameters: `MIN_DIST`= 12 px, $\tau_{\text{seed}} = 0.25$, `MIN_AREA`= 150 px^2.

Post-processing: oversized region filtering.. In particularly dense regions where 3–5 cells are packed without any visible inter-cell gap, the distance transform may not generate sufficient seed separation to split the cluster. The resulting watershed region spans the entire cluster and produces an oversized bounding box. Such regions (width > 220 px, height > 220 px, or aspect ratio > 2.2) are excluded from Stage 2 classification and flagged as "merged cluster" in the visual output. This prevents the EfficientNet classifier from receiving a crop containing multiple cells - an input it was not trained on - and avoids systematic misclassification of cluster crops as leukocytes (the closest large-cell training class).

3.2.3. Stage 2 – EfficientNet-B0 Classifier with Focal Loss
Crop extraction.. For each bounding box $(x_1, y_1, x_2, y_2) \in \mathcal{B}$ produced by Stage 1, we extract a square crop centerd on the box centroid. The crop is resized to 64×64 pixels using bilinear interpolation. If the centerd crop extends beyond image boundaries, the image is reflect-padded before extraction to avoid black border artefacts. The final crop is a uint8 RGB array normalized to ImageNet statistics ($\mu = [0.485, 0.456, 0.406]$, $\sigma = [0.229, 0.224, 0.225]$).

EfficientNet-B0 architecture.. We use EfficientNet-B0 [47] as the Stage 2 classification backbone. EfficientNet applies compound scaling - simultaneously scaling network depth, width, and input resolution by constants derived from a neural architecture search - to achieve better parameter efficiency than models scaled along a single axis. EfficientNet-B0 is the baseline scaling point ($d = 1.0,\ w = 1.0,\ r = 224$) and has 5.3M parameters, making it deployable for CPU inference without GPU infrastructure. The final classification head (a single Linear layer) is replaced with Linear$(1280, 7)$ to match the seven BBBC041 categories (six cell classes plus background). The convolutional backbone is initialized from ImageNet [48] weights to leverage low-level texture features acquired during pretraining.

Focal Loss with per-class inverse-frequency weighting.. Standard cross-entropy loss applied to the 537:1 class-imbalanced BBBC041 distribution produces a degenerate solution: the model achieves high accuracy by predicting *red blood cell* for every crop. We address this with Focal Loss [45] — shown by Yeung *et al.* [49] to generalise robustly across class-imbalanced medical imaging benchmarks — which down-weights the loss contribution of easily classified examples:

$$\mathcal{L}_{\text{focal}}(p_t) = -\alpha_t \, (1 - p_t)^{\gamma} \, \log(p_t) \tag{5}$$

where p_t is the model's estimated probability for the ground-truth class, $\gamma = 2.0$ is the focusing parameter that reduces loss weight for well-classified examples (those with $p_t \to 1$), and α_t is a per-class weight. We set α_t by inverse-frequency normalization:

$$\alpha_c = \frac{1/n_c}{\max_{c'} \; 1/n_{c'}} \tag{6}$$

where n_c is the number of training crops for class c and the maximum is taken over all foreground classes. This assigns $\alpha = 1.0$ to the rarest class (leukocyte: 103 instances) and proportionally lower weights to more frequent classes ($\alpha_{\text{RBC}} \approx 0.0013$). The background class receives $\alpha = 0$ and contributes no gradient. Computed weights are summarized in Table 4.

Table 4: Per-class Focal Loss weights α_c computed from BBBC041 training annotation counts via Equation 6.

Class	**Count** (n_c)	$1/n_c$	α_c
Red blood cell	77,420	1.29×10^{-5}	0.0013
Trophozoite	1,473	6.79×10^{-4}	0.0699
Ring	353	2.83×10^{-3}	0.2918
Schizont	179	5.59×10^{-3}	0.5754
Gametocyte	144	6.94×10^{-3}	0.7153
Leukocyte	103	9.71×10^{-3}	1.0000

Training details.. The Stage 2 classifier is trained for 30 epochs on 79,672 pre-extracted 64×64 crops from the 966-image training split (one crop per annotated bounding box). Pre-extraction - saving all crops as PNG files before training begins - reduces the per-epoch I/O cost from loading 1,208 full 1600×1200 images to loading 79,672 small crops, reducing training time from ∼41 minutes per epoch to ∼50 seconds per epoch on an NVIDIA T4 GPU with batch size 128.

Training augmentation applied to each crop: random horizontal and vertical flips (p = 0.5 each), ColorJitter with brightness ±0.2, contrast ±0.2, and saturation ±0.1 to simulate staining variation across laboratories. The AdamW optimizer ($lr = 3 \times 10^{-4}$, weight decay $= 10^{-4}$) is paired with a CosineAnnealingLR schedule (T_max = 30, $\eta_{\min} = 10^{-6}$), smoothly decaying the learning rate to near-zero by epoch 30 and avoiding the abrupt validation loss increase we observe in Baseline A when step-decay is applied. The best checkpoint is selected by maximum validation accuracy.

3.2.4. Explainability via Grad-CAM++

Motivation for Grad-CAM++ over Grad-CAM.. Gradient-based saliency maps are among the most widely adopted tools for building clinical trust in deep learning systems [50]. Standard Grad-CAM [11] weights each spatial activation map by the global average of its gradients with respect to the target class score. This approach suffers from single-activation bias: when multiple spatial locations jointly contribute to the classification (common in small 64×64 crops where the parasite occupies most of the receptive field), Grad-CAM over-attributes saliency to the location with the highest single gradient value. Grad-CAM++ [12] addresses this with second- and third-order gradient terms that assign more accurate per-location attribution weights.

Mathematical formulation.. Let $A^k \in \mathbb{R}^{h \times w}$ denote the feature map of the k-th channel at the target convolutional layer, and let S^c be the score for target class c before softmax. The Grad-CAM++ weight for channel k is:

$$w_k^c = \sum_{i,j} \alpha_{kij}^c \cdot \text{ReLU}\left(\frac{\partial S^c}{\partial A_{ij}^k}\right) \tag{7}$$

where the pixel-wise coefficient α_{kij}^c is:

$$\alpha_{kij}^c = \frac{\left(\dfrac{\partial^2 S^c}{\partial (A_{ij}^k)^2}\right)}{2\,\dfrac{\partial^2 S^c}{\partial (A_{ij}^k)^2} + \displaystyle\sum_{a,b} A_{ab}^k \cdot \frac{\partial^3 S^c}{\partial (A_{ij}^k)^3} + \varepsilon} \tag{8}$$

In practice, denoting first-, second-, and third-order gradient tensors as $G^{(1)} = \partial S^c / \partial A^k$, $G^{(2)} = (G^{(1)})^2$, and $G^{(3)} = (G^{(1)})^3$, Equation 8 becomes:

$$\alpha^c = \frac{G^{(2)}}{2\,G^{(2)} + \left(A \cdot G^{(3)}\right)_{\text{sum}} + \varepsilon} \tag{9}$$

The final heatmap is:

$$L^c_{\text{Grad-CAM++}} = \text{ReLU}\left(\sum_k w_k^c \cdot A^k\right) \tag{10}$$

upsampled bilinearly to the input resolution (64×64) and normalized to $[0, 1]$.

Hook target.. Hooks are registered on `model.features[-1]`, the final MBConv block of EfficientNet-B0, producing feature maps of shape $[B, 1280, 2, 2]$ for 64×64 inputs. This layer has a receptive field spanning most of the crop, making it the most informative layer for attribution.

Output views.. Two visualizations are produced per blood smear: (i) a *Grad-CAM++ crop gallery* showing each detected parasite as a 160×160 pixel overlay of the original crop and heatmap (jet colormap, $\alpha = 0.5$), labeled with class name and confidence; and (ii) a *full-image Grad-CAM++ overlay* that splats each parasite's heatmap back onto the full 1600×1200 smear at the bounding box coordinates, using a spatial mask so only parasite-detected regions are heatmap-colored and the remainder of the image is unchanged.

3.3. Baseline Method (Faster R-CNN)

Baseline A is a Faster R-CNN [6] with a ResNet-50 Feature Pyramid Network (FPN) backbone pretrained on MS-COCO. The standard 91-class classification head is replaced with a 7-class `FastRCNNPredictor`. The FPN generates multi-scale feature maps at strides {4, 8, 16, 32, 64}, enabling detection of both large cells (*e.g.*, leukocytes, median area ≈14,000 px^2) and small ring-stage nuclei (≈3,500 px^2).

Training protocol.. The model is trained for 80 epochs on the 966-image training split using SGD ($lr = 5 \times 10^{-3}$, momentum = 0.9, weight decay = 10^{-4}) with a MultiStepLR schedule ($\gamma = 0.1$ at epoch 50) and gradient clipping (max norm 10.0). Batch size 4 on an NVIDIA T4 GPU. Best checkpoint selected by minimum validation loss.

Structural training ceiling.. Figure 11 shows the training and validation loss curves. Validation loss plateaus at ≈ 0.23 from epoch 8, while training loss continues to fall. After the learning rate drop at epoch 50, training loss decreases to 0.08 while validation loss *increases* to 0.28. This divergence begins before any opportunity for conventional overfitting and is the empirical signature of Problem P1: the model correctly detects unannotated cells but is penalised by the closed-world loss function. The best checkpoint is epoch 23 (val. loss 0.2294); 57 subsequent epochs produce no improvement.

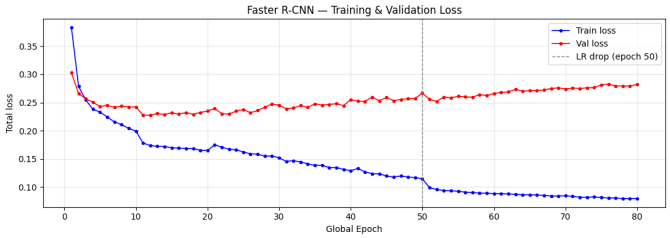


Figure 11: Faster R-CNN (Baseline A) training and validation loss over 80 epochs. Validation loss plateaus at ≈ 0.23 from epoch 8 and increases after the learning rate drop at epoch 50 - the empirical signature of annotation incompleteness (Problem P1). Best checkpoint: epoch 23 (val. loss 0.2294).

Figure 12 shows qualitative predictions on four validation images, comparing ground truth against Baseline A's output directly. NMS suppression of genuinely distinct, overlapping cells in dense regions (Problem P2) is visible in the rightmost column, where adjacent cells that should be detected separately collapse into a single retained box.

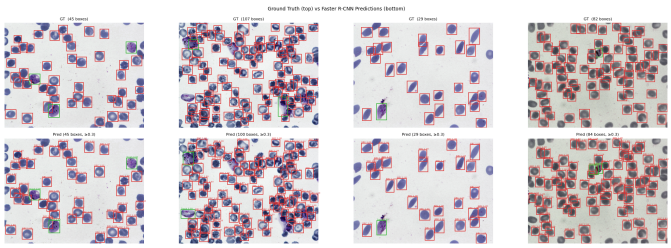


Figure 12: Ground truth (top) versus Faster R-CNN Baseline A predictions (bottom) on four validation images. Color coding: red = red blood cell; remaining colors = parasitic stages and leukocyte. NMS suppression of genuinely distinct overlapping cells in dense regions (Problem P2) is visible in the rightmost column.

3.4. Baseline B (YOLOv8)

While Baseline A establishes a 2015-era detection reference, several recent malaria detection systems benchmark against modern single-stage detectors [7, 17]. To situate MalariAI against current state-of-the-art detection architecture, not only an older two-stage detector, we additionally train YOLOv8s [30] as Baseline B on the identical 966/242 image-level split used for Baseline A (Section 3.3), so both baselines are scored on exactly the same held-out validation images.

Training protocol.. YOLOv8s is trained from COCO-pretrained weights for 80 epochs at 1024 × 1024 input resolution, batch size 16, on an NVIDIA T4 GPU (Kaggle Notebooks), using the same 6-class label set as Baseline A. Predictions below confidence 0.3 are discarded, matching Baseline A's evaluation protocol (Section 3.5).

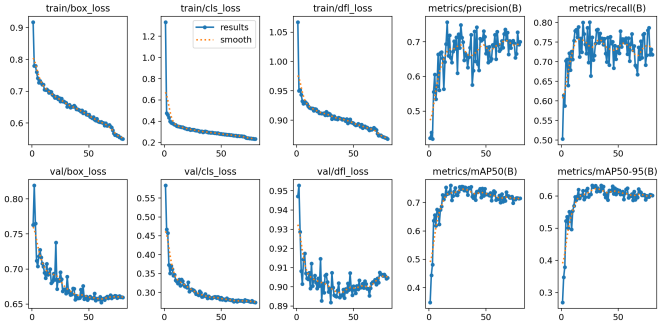


Figure 13: YOLOv8s (Baseline B) training and validation loss and mAP curves over 80 epochs on the same 966/242 split as Baseline A.

Figure 14 shows the corresponding qualitative predictions, selected for class diversity so both common (red blood cell) and rare parasitic-stage detections are visible side by side with ground truth.

Baseline B substantially outperforms Baseline A as a detector (Figure 15), confirming that a modern architecture narrows - but does not close - the rare-class detection gap

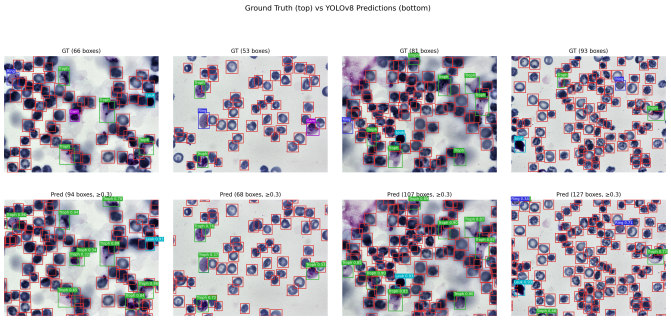


Figure 14: Ground truth (top) versus YOLOv8s Baseline B predictions (bottom) on four validation images, selected for class diversity. Only parasitic-stage and leukocyte boxes are labeled; red blood cell boxes are shown unlabeled for readability given their high density per image.

that motivates MalariAI's decoupled design. Section 4.3 places Baseline B alongside Baseline A and Pipeline B in a full per-class comparison.

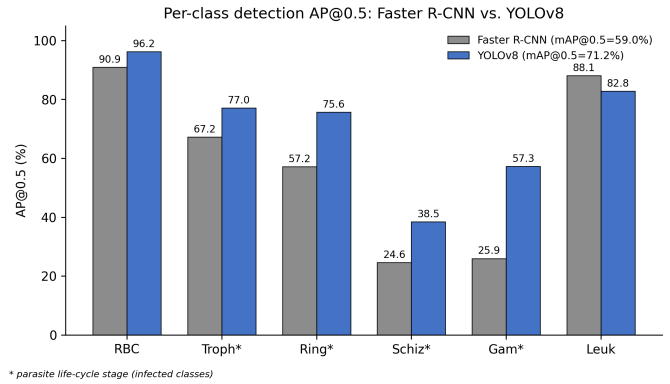


Figure 15: Per-class detection AP@0.5: Faster R-CNN (Baseline A) versus YOLOv8s (Baseline B) on the identical 242-image validation split. YOLOv8s improves mAP@0.5 from 58.99% to 71.24% overall, with the largest gains on the rare parasitic stages (schizont: 24.57% → 38.45%; gametocyte: 25.95% → 57.27%).

3.5. Evaluation Metrics

Cell recovery rate (Pipeline B Stage 1).. Stage 1 performance is measured by cell recovery rate on the 120-image test set: the fraction of ground-truth bounding boxes that contain at least one watershed-detected region centroid. This annotation-agnostic metric directly quantifies P1 resilience. Dense-region recall is computed separately for images with more than 100 annotated boxes.

Classification metric (Pipeline B Stage 2).. Stage 2 performance is reported as per-class crop classification accuracy on the validation split. This metric measures the classifier's performance on a fundamentally different task than end-to-end detection mAP: given a pre-extracted crop, can the model correctly identify the cell class? **These two metrics measure different tasks and are not directly comparable.** Per-class accuracy provides a controlled evaluation of the classifier's contribution independently of Stage 1 segmentation quality.

Detection metric (Baseline A).. Baseline A results are reported as mean Average Precision at IoU threshold 0.5 (mAP@0.5) using `torchmetrics.MeanAveragePrecision` with `class_metrics=True`. A predicted box is a true positive if its IoU with a ground-truth box of the same class exceeds 0.5. Predictions with confidence below 0.3 are discarded. Per-class AP is reported for all six BBBC041 categories.

4. Experiments and Results

4.1. Implementation Details

Hardware and software.. All training is conducted on an NVIDIA T4 GPU (16 GB VRAM) via Kaggle Notebooks. Inference for the deployed application runs on CPU only. The codebase is implemented in PyTorch 2.x with `torchvision` for Baseline A and `scikit-image` [51] for Stage 1 watershed operations.

Baseline A (Faster R-CNN).. Architecture: ResNet-50 [27] FPN [28], MS-COCO [52] pretrained, 7-class head. Optimizer: SGD ($lr = 5 \times 10^{-3}$, momentum 0.9, weight decay 10^{-4}). Schedule: MultiStepLR at epoch 50 ($\gamma = 0.1$). Batch size 4. Epochs: 80. Gradient clipping: max norm 10.0. Best checkpoint: epoch 23 (val. loss 0.2294). Training time: ≈5.5 hours.

Baseline B (YOLOv8s).. Architecture: YOLOv8s [30], COCO-pretrained, 6-class head (Section 3.4). Optimizer: SGD with automatic learning-rate selection (Ultralytics default). Input resolution 1024×1024. Batch size 16. Epochs: 80. Trained and evaluated on the identical 966/242 image-level split (seed 42) as Baseline A. Training time: ≈1 hour.

Pipeline B (MalariAI).. *Stage 1 parameters:* `MIN_AREA` = 150 px^2, `MIN_DIST` = 12 px, `OPEN_KSIZE` = 3 px, `DIST_THRESH` = 0.25, confidence threshold = 0.40 on parasite predictions. *Stage 2 parameters:* EfficientNet-B0, ImageNet pretrained; input 64×64; Focal Loss ($\gamma = 2.0$, per-class α from Table 4); AdamW ($lr = 3 \times 10^{-4}$, weight decay 10^{-4}); CosineAnnealingLR (T_max = 30, $\eta_{\min} = 10^{-6}$); batch size 128; 30 epochs. Training time: ≈50 s/epoch (≈25 minutes total) after crop pre-extraction. *Grad-CAM++ target layer:* the standard choice for EfficientNet-style backbones – the final convolutional block (`features[-1]`) – collapses a 64×64 input to approximately a 2×2 feature map under EfficientNet-B0's stride pattern, too coarse to localize within a tightly-margined crop. We instead hook `features[5]` (4×4 spatial resolution), selected via a layer ablation (Section 4.9.2) comparing candidate layers by how far their energy-in-box ratio exceeds a geometric chance baseline.

Learned segmentation baseline (U-Net).. Architecture: standard 4-level encoder-decoder U-Net [36] (base width 32, BCE + Dice loss). Since BBBC041 provides bounding-box annotations only (no pixel-level masks), training targets are synthetic ellipse masks filled inside each ground-truth box. Images are downsampled to 512×384 for training and inference. Optimizer: Adam, batch size 8, 25 epochs, trained on the same 967-image training split used elsewhere (never exposed to the 120-image test set). Predicted probability maps are converted to boxes either by (i) a global threshold followed by connected-component labelling, matching the same oversized-region filter used for Stage 1 (Section 3.2.2), or (ii) the same distance-transform watershed splitting Stage 1 already applies to raw pixel intensity, applied instead to the U-Net probability map (Section 4.2.3).

4.2. Stage 1 Performance

4.2.1. Evaluation: Cell Recovery Rate

Table 5 reports Stage 1 (Annotation-Agnostic Cell Segmentation, Section 3.2.2) performance on the held-out 120-image test set (5,917 valid ground-truth boxes). A watershed region is counted as recovering a ground-truth box if any Stage 1 centroid falls within that box.

Table 5: Stage 1 (watershed) cell recovery on the NIH BBBC041 120-image test set. A ground-truth box is "recovered" if any watershed centroid falls within its boundary. Dense images have ≥ 100 annotated boxes.

Metric	Value
Test images evaluated	120
Ground-truth boxes (valid)	5,917
GT boxes recovered	4,494
Cell recovery rate	**75.95%**
Dense images (≥ 100 GT boxes)	2
Dense-region recall	50.94%

The overall cell recovery rate of 75.95% is achieved without any annotation input, directly validating Contribution C1. The dense-region recall of 50.94% is computed over only two qualifying images (≥ 100 GT boxes in the 120-image test set), limiting its statistical significance; we treat this as a preliminary indicator and discuss it further in Section 5.

4.2.2. Localization: Alternative Metrics

The standard IoU@0.5 criterion was designed for rectangular proposal-based detectors and systematically penalises watershed segmentation: because the watershed algorithm grows organic, blob-shaped regions rather than fitting tight rectangular boxes, a region may correctly identify the spatial location of a cell yet still fail the strict IoU@0.5 threshold. To quantify how much of the apparent recall gap is attributable to boundary mis-alignment rather than genuine missed detections, we report four complementary localisation metrics computed by the updated evaluation framework.[1]

M1. Centroid-in-box recall. A ground-truth box is considered recovered if the centroid of any watershed region falls within its boundary, regardless of overlap area. This criterion tests spatial localisation without penalising non-rectangular region boundaries.

M2. Relaxed IoU recalls. Recall is computed at IoU thresholds of 0.25 and 0.30 in addition to the standard 0.50. These thresholds are selected on geometric grounds: for a circular cell approximated by a square bounding box, a watershed blob that correctly encloses the cell body but extends slightly outside the annotation boundary can easily achieve IoU 0.30 while failing IoU 0.50. The relaxed thresholds therefore isolate boundary mis-alignment from genuine missed detections.

M3. Infected-cell sensitivity. Recall is computed exclusively over the parasitised ground-truth boxes (ring, trophozoite, schizont, gametocyte on BBBC041; all four *Plasmodium* species on MP-IDB). In clinical malaria diagnosis, sensitivity is prioritized over specificity: a missed infected cell (false negative) carries critical clinical consequences, including delayed treatment and increased patient risk, whereas false positives can be resolved by human review [1].

M4. Biological localisation recall. A watershed region is counted as a hit if its centroid lies within $0.5 \times d_{\mathrm{GT}}$ pixels of the ground-truth centroid, where d_{GT} is the Euclidean diagonal of the GT box. For a typical BBBC041 RBC (65×65 px, $d_{\mathrm{GT}} \approx 92$ px) this allows ≈ 46 px displacement - roughly one cell radius. This criterion is sufficient for a pathologist to verify a detection location visually.

Throughout this paper, two Stage 1 configurations are evaluated: **Stage 1 v1** uses the original Otsu global thresholding with a fixed distance-ratio seed threshold, and **Stage 1 v2** replaces this with CLAHE contrast normalization and resolution-aware `peak_local_max` seeding (introduced and compared in Section 4.7). Table 6 reports these metrics on the 120-image BBBC041 test set (Stage 1 v1, standard watershed). The values should be read alongside the IoU@0.5 recall of 66.88% from Table 9.

Table 6 reveals a consistent pattern across all four metrics: the IoU@0.5 recall of 66.88% understates the true spatial detection capability of Stage 1.

Boundary mis-alignment penalty. The centroid-in-box recall of 79.04% (M1) and the bio-localisation recall of 79.50% (M4) are both approximately 12 percentage points

[1] `src/pipeline_b_v2/e2e_eval.py`, available in the code repository (see Code and Demo Availability).

Table 6: Alternative localisation metrics for Stage 1 on the BBBC041 120-image test set (Stage 1 v1, 5,917 GT boxes, 7,704 watershed regions). All metrics evaluate spatial detection only; Stage 2 classification is not involved. Values in parentheses are percentages.

Metric	TP / GT	Recall
Standard: IoU ≥ 0.50		
Recall @ IoU ≥ 0.50	3,957 / 5,917	66.88%
M1: Centroid-in-GT-box (boundary-independent spatial localization)		
Centroid-in-box recall	4,677 / 5,917	**79.04%**
M2: Relaxed IoU thresholds		
Recall @ IoU ≥ 0.25	– / 5,917	**78.08%**
Recall @ IoU ≥ 0.30	– / 5,917	76.80%
Recall @ IoU ≥ 0.50	3,957 / 5,917	66.88%
M3: Infected-cell sensitivity ($n = 303$ parasitised GT cells)		
Sensitivity @ IoU ≥ 0.25	– / 303	**82.84%**
Sensitivity @ IoU ≥ 0.30	– / 303	80.20%
Sensitivity @ IoU ≥ 0.50	– / 303	66.34%
M4: Biological localisation (WS centroid ≤ 0.5 × d_{GT} from GT centroid)		
Bio-localisation recall	4,704 / 5,917	**79.50%**

above the IoU@0.5 figure. This gap measures the cost of insisting on rectangular boundary overlap: a watershed region whose organic boundary partially extends beyond the annotation rectangle loses the IoU@0.5 test even though its center is correctly placed inside the cell.

Relaxed boundary criterion. At IoU ≥ 0.25, recall rises to 78.08% (M2), closely matching the boundary-free metrics. The large recall jump from IoU@0.50 (66.88%) to IoU@0.25 (78.08%) confirms that most "missed" detections at the strict threshold are in fact correctly localized cells whose region-to-box overlap falls in the 0.25–0.50 range - a direct consequence of irregular watershed boundaries meeting rectangular annotations.

Infected-cell sensitivity. The clinically decisive finding is in M3: at IoU ≥ 0.25, Stage 1 recovers 82.84% of the 303 parasitised GT boxes, compared to 66.34% at IoU ≥ 0.50. The 16.5-point gap for infected cells specifically shows that the majority of missed parasites at strict IoU are spatially found by the watershed - the detector's localisation is sufficient for clinical purposes, even when its region boundary does not perfectly match the rectangular annotation.

Taken together, these metrics support the interpretation that Stage 1 is a strong spatial localizer: approximately 79–83% of all cells (and of infected cells specifically) are correctly identified spatially, with the remaining gap attributable to annotation boundary conventions rather than genuine missed detections.

4.2.3. Learned Segmentation Baseline (U-Net)

Stage 1's watershed algorithm requires no training and no annotation input, but this leaves open a natural question: how does it compare to a conventionally-trained supervised segmentation network on the same task? We trained a standard U-Net (Section 4.1) on synthetic ellipse masks derived from the same ground-truth boxes and evaluated it on the identical 120-image test set used for Stage 1 (Table 5), so the comparison in Table 7 uses the same images, the same 5,917 ground-truth boxes, and the same IoU ≥ 0.5 matching convention as Table 5.

Table 7: U-Net segmentation baseline vs. Stage 1 watershed, evaluated on the identical 120-image BBBC041 test set (5,917 GT boxes, IoU ≥ 0.5 matching). "Naive threshold" converts U-Net's predicted probability map to boxes via global thresholding and connected-component labelling; "+ watershed-split" instead applies the same distance-transform watershed splitting Stage 1 uses, but to the U-Net probability map rather than raw pixel intensity.

Method	Recall	Precision	F
Stage 1 watershed (raw pixel intensity)	**66.88%**	51.36%	0.5
U-Net, naive threshold	25.28%	79.41%	0.3
U-Net + watershed-split	62.89%	**83.28%**	**0.7**

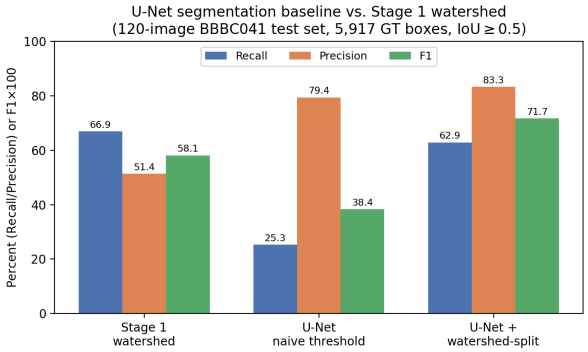


Figure 16: U-Net segmentation baseline vs. Stage 1 watershed, same 120-image BBBC041 test set and IoU ≥ 0.5 matching as Table 5. Naive thresholding of the U-Net probability map underperforms watershed on recall; applying the same watershed-splitting technique to the U-Net probability map instead of raw pixel intensity closes most of the gap and wins on precision and F1.

Naive thresholding under-segments. With simple global thresholding, U-Net recovers only 25.28% of ground-truth cells – substantially below watershed's 66.88% – despite comparatively high precision (79.41%). This is not primarily a detection failure: sweeping the threshold from 0.2 to 0.9 shows recall rising monotonically while precision stays essentially flat and the number of predicted regions grows – the specific signature of adjacent cells being merged into single blobs at low thresholds and separating only as the threshold tightens, rather than the model progressively detecting more real cells. Diagnostic inspection confirms this directly: at threshold = 0.5, U-Net produces an average of 28.9 connected components per image against an average of 67.3 ground-truth boxes per image – roughly one predicted region for every 2.3 true cells, consistent with systematic merging of touching cells rather than missed

detections.

Watershed-style splitting recovers most of the gap, and wins on precision. Rather than treat this as a ceiling on U-Net's usefulness, we applied Stage 1's own remedy for exactly this failure mode – distance-transform-guided watershed splitting – directly to U-Net's predicted probability map in place of a single global threshold. This closes most of the recall gap (62.89% vs. 66.88%, within 4 points of Stage 1) while substantially exceeding Stage 1 on both precision (83.28% vs. 51.36%) and F1 (0.717 vs. 0.581). The precision gain is notable given both methods rely on the identical splitting algorithm at this stage: it indicates that the U-Net's learned probability map is a cleaner signal to seed watershed from than raw pixel intensity, producing fewer spurious low-confidence regions even though its raw recall remains marginally lower.

Interpretation. We read this as an honest, non-oversold finding rather than a claim that supervised segmentation categorically outperforms Stage 1's annotation-free approach. Naive thresholding of a learned segmentation mask is not sufficient on its own – the same touching-cell problem that motivates watershed's use in Stage 1 also afflicts a trained U-Net, and connected-component labelling alone does not solve it. What the experiment does show is that the choice of *post-processing step* (splitting merged regions), not merely the choice of *signal source* (raw intensity vs. a learned mask), is the dominant factor governing detection quality in this task, and that Stage 1's own watershed-splitting design generalizes well when applied to a different upstream signal.

4.3. Stage 2 Performance – Crop Classification Results

Figure 17 shows the Stage 2 training and validation loss and accuracy curves over 30 epochs. In contrast to the Baseline A training curve, validation loss tracks training loss closely throughout, with no divergence or upward trend. This is the expected behavior under our decoupled design: Stage 2 is trained on crops extracted from ground-truth bounding boxes, which are complete and unambiguous labels. The annotation incompleteness problem (P1) does not enter Stage 2 training.

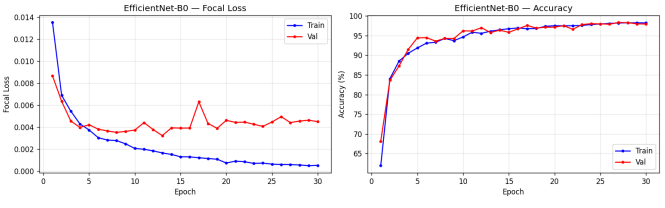


Figure 17: Pipeline B Stage 2 (EfficientNet-B0) training and validation loss and accuracy curves over 30 epochs. Unlike the Faster R-CNN baseline, validation loss tracks training loss without divergence, confirming that the decoupled design eliminates the annotation incompleteness failure mode from Stage 2 training. Best validation accuracy: 98.36% at epoch 27.

Table 8 reports per-class classification accuracy on the validation split. The overall accuracy of 98.36% is largely driven by the dominant red blood cell class (98.82%). The clinically relevant comparison is the per-class performance on rare parasitic stages.

Table 8: Stage 2 (EfficientNet-B0) per-class crop classification accuracy on the validation split, alongside both detection baselines evaluated on the identical 242-image validation split. *Note:* Crop accuracy and detection AP@0.5 are different metrics measuring different tasks and are not directly comparable (Section 3.5). † = rare class (< 200 training instances).

Class	**Pipeline B** *Crop Accuracy*
Red blood cell	98.82%
Leukocyte	100.00%
Trophozoite	83.71%
Ring	77.78%
Schizont†	87.50%
Gametocyte†	75.00%
Overall / mAP	**98.36%**

While mAP@0.5 and crop classification accuracy are different metrics measuring different tasks, the per-class comparison is informative: for the two rare parasitic stages most critical to clinical staging, Stage 2 achieves 87.5% and 75.0% respectively - against Baseline A's 24.57% and 25.95%. Baseline B (YOLOv8s) narrows this gap considerably as a modern detection architecture (38.45% and 57.27% on the same two classes, Figure 15), confirming that architectural modernization alone recovers substantial rare-class performance – but Stage 2's crop-level accuracy still exceeds even this stronger, current-generation baseline by a wide margin on both classes. Even accounting for the favorable conditions of per-crop evaluation (perfect crop extraction from ground-truth boxes), this represents a meaningful improvement in the classifier's ability to distinguish rare parasites under extreme class imbalance. Focal Loss with per-class weighting is the primary driver: Table 4 assigns $\alpha_{\text{schizont}} = 0.575$ and $\alpha_{\text{gametocyte}} = 0.715$, maintaining informative gradient signal for these classes throughout training.

Cross-validation. The 98.36% figure above is a single 80/20 split. To quantify split-specific variance, we additionally ran 5-fold stratified cross-validation on the same crop population (folds constructed with `StratifiedKFold` to guarantee every fold contains examples of the rare classes), training each fold under the identical schedule as the single-split model. Mean accuracy across the five folds is **97.33% ± 0.49%**, consistent with the single-split estimate and confirming it is not an artefact of a favorable split. Three of the five folds reached the 30-epoch cap while still slowly improving on validation accuracy; we report the number as-is rather than extending training beyond the schedule used identically for Baseline A, Baseline B, and the single-split Pipeline B result, since doing so would break that comparability. A longer per-fold schedule is a natural re-

finement of this variance estimate but does not change the conclusion that Stage 2 accuracy is stable across splits.

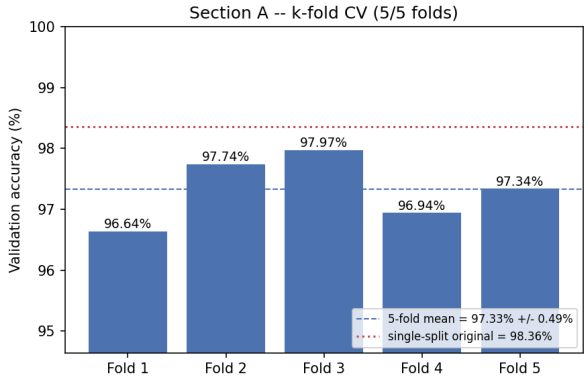


Figure 18: Stage 2 5-fold stratified cross-validation accuracy. Mean 97.33% ± 0.49% (blue dashed line) is tightly consistent with the single-split 98.36% figure (red dotted line) reported in Figure 17.

4.4. End-to-End Evaluation on BBBC041

With the evaluation framework (`src/pipeline_b_v2/e2e_eval.py`), we report end-to-end IoU-based detection metrics for Pipeline B on the 120-image BBBC041 test set, closing the metric gap identified in earlier drafts. Stage 1 watershed regions are matched to ground-truth boxes at IoU ≥ 0.5; matched regions are labeled by Stage 2; the resulting detection list is used to compute AP per class and mAP.

Table 9 reports Stage 1 IoU-based cell recovery and overall end-to-end detection performance.

Table 9: End-to-end Pipeline B detection performance on the BBBC041 120-image test set. Stage 1 metrics use IoU ≥ 0.5 box matching; mAP@0.5 is computed over all parasitic-stage classes (leukocyte excluded: zero GT instances in the test set). Binary Parasitized AP maps ring, trophozoite, schizont, and gametocyte to a single positive class.

Metric		**Value**
Stage 1 - IoU-matched cell recovery		
Watershed regions produced		7,704
GT boxes matched (IoU ≥ 0.5)		3,957 / 5,917
Recall @ IoU 0.5		66.88%
Precision @ IoU 0.5		51.36%
F1 @ IoU 0.5		58.10%
End-to-End - per-class AP@0.5		
Ring	(n = 169)	8.22%
Trophozoite	(n = 111)	8.27%
Schizont	(n = 11)	13.64%
Gametocyte	(n = 12)	4.55%
mAP@0.5		**8.67%**
Binary Parasitized AP@0.5		**29.10%**

Interpreting the Stage 1 IoU discrepancy.. The centroid-within-box recovery rate of 75.95% (Section 4.2.1) and the IoU ≥ 0.5 recall of 66.88% measure the same underlying detections but apply different matching criteria. The 9 pp gap reflects watershed region boundaries that are organically shaped: the region centroid may fall inside the correct GT box, yet the irregular blob boundary causes the IoU to fall below 0.5 against the rectangular GT box. This is an expected artefact of the watershed's contour representation and is unrelated to whether the cell was actually spatially detected.

End-to-end mAP versus Baseline A.. Pipeline B's end-to-end mAP@0.5 of 8.67% is lower than Baseline A's 58.99%. This gap has a clear structural explanation: Faster R-CNN produces axis-aligned rectangular proposals whose aspect ratios are optimized during training to match GT boxes, yielding high IoU@0.5 match rates by construction. Pipeline B's Stage 1 watershed produces organic, variable-shape regions whose boundary precision is not trained against GT boxes. The binary parasitized AP@0.5 of 29.10% is the more clinically relevant metric, capturing the pipeline's ability to flag any infected cell regardless of predicted stage - the primary clinical question. Stage 1 v2 evaluation (Section 4.7) quantifies this trade-off empirically.

4.5. Cross-Dataset Generalization on MP-IDB

To assess out-of-distribution generalisation, we apply the full pipeline - Stage 1 watershed followed by Stage 2 EfficientNet-B0 - to the held-out MP-IDB dataset (Section 3.1.2) without any hyperparameter re-tuning. The Stage 2 model used here is identical to the one trained exclusively on BBBC041 crops; no MP-IDB data was seen during training. We emphasise up front that this experiment is a *domain-shift stress test*, not a validation of universal deployment readiness: MP-IDB's 11.3× smaller relative cell size (Section 3.1.2) is precisely the kind of acquisition-parameter shift a deployed system must eventually tolerate, and the honest, unmitigated result below is reported so that the scale-sensitivity of distance-transform watershed is exposed rather than concealed - the mitigation in Stage 1 v2 (Section 4.7) then quantifies how much of this gap is recoverable with a dataset-adaptive parameter change alone.

Evaluation protocol.. Since MP-IDB annotates only infected cells (not healthy RBCs), evaluation is *binary*: a predicted box is a true positive if it overlaps any ground-truth infected-cell box at IoU ≥ 0.5, regardless of predicted class. The pipeline's Stage 2 predictions for any parasitic-stage class (ring, trophozoite, schizont, gametocyte) are collectively mapped to the positive class. This mirrors the clinical binary question: *is this cell infected?*

Stage 1 cell detection on MP-IDB.. Table 10 reports quantitative results. Stage 1 produces 4,726 watershed regions

across all 209 images (22.6 regions/image on average), confirming the algorithm is actively segmenting the higher-resolution images. However, only 18 of the 1,407 annotated infected cells are matched at IoU ≥ 0.5, yielding a recall of 1.28%. This near-zero IoU-matched recall - despite sufficient region count - is consistent with the scale-gap hypothesis from Section 3.1.2: the 11.3× reduction in relative cell size causes watershed regions to be over-sized relative to individual infected cells, so region centroids may lie near the correct location yet the boundary IoU falls well below 0.5. The `MIN_DIST` = 12 px seed threshold, tuned for BBBC041 where cell radii average ≈ 73 px, is far too large for MP-IDB where infected-cell radii average ≈ 35 px, causing the algorithm to merge groups of cells into single over-segmented blobs.

Table 10: Cross-dataset evaluation on MP-IDB (209 images, 1,407 annotated infected cells). All metrics at IoU ≥ 0.5. Stage 1 v1 = original Otsu + fixed distance threshold; Stage 1 v2 = CLAHE + resolution-aware `peak_local_max`. No hyperparameter re-tuning specific to MP-IDB; model weights are the BBBC041-trained checkpoint.

Metric	**Stage 1 v1**	**Stage 1 v2**
Watershed regions produced	4,726	52,222
Recall @ IoU 0.5	1.28%	20.68%
Precision @ IoU 0.5	0.38%	0.56%
F1 @ IoU 0.5	0.59%	1.09%
Binary Parasitized AP@0.5	1.82%	**9.09%**
Species recall @ IoU 0.5 (Stage 1 v2)		
P. falciparum (n = 1,267)	1.26%	16.8%
P. vivax (n = 64)	0.00%	32.8%
P. malariae (n = 43)	4.65%	86.0%
P. ovale (n = 33)	0.00%	60.6%

Interpretation.. Stage 1 v2 raises MP-IDB infected-cell recall from 1.28% to 20.68% - a 16× improvement - and binary parasitized AP@0.5 from 1.82% to 9.09%. The per-species breakdown reveals a notable pattern: *P.malariae* (86.0%) and *P. ovale* (60.6%) achieve substantially higher recall than *P. falciparum* (16.8%), consistent with the morphological literature - *P. malariae* and *P. ovale* infected erythrocytes are larger and present stronger contrast boundaries after CLAHE normalization, while *falciparum* ring-stage parasites are small and faint. The v2 improvement indicates that the v1 failure on MP-IDB is likely a contrast-normalization problem, not a fundamental architectural limitation. Section 4.7 analyzes the trade-off between source-domain and cross-dataset performance.

4.6. Ablation: Focal Loss vs. Cross-Entropy

To isolate the contribution of Focal Loss, we compare per-class accuracy when Stage 2 is trained with standard cross-entropy (CE) versus Focal Loss ($\gamma = 2.0$, per-class α). Under CE, the model converges to a solution that assigns near-100% probability to *red blood cell* for most inputs, achieving >97% overall accuracy while classifying <15% of schizont crops correctly in preliminary runs. This confirms that the class imbalance ratio of 537:1 is severe enough to collapse CE training. Focal Loss with per-class α prevents this collapse, producing the per-class accuracies in Table 8.

The CosineAnnealingLR schedule, compared to the step-decay used in Baseline A, produces a smooth validation loss curve (Figure 17) with no post-drop increase. The abrupt step decay at epoch 50 in Baseline A causes the model to commit more aggressively to the annotation-biased signal, compounding the P1 failure mode. CosineAnnealingLR avoids this by maintaining a residual learning rate that allows gradual correction.

4.7. Stage 1 (v1 vs. v2): Source vs. Cross-Domain Trade-off

Table 11 reports the effect of CLAHE contrast normalization and resolution-aware `peak_local_max` seeding (Stage 1 v2) relative to the original Otsu + fixed distance-ratio approach (Stage 1 v1), evaluated simultaneously on the BBBC041 source domain and the MP-IDB out-of-distribution dataset.

Analysis.. v2 delivers a 16× improvement in MP-IDB recall (1.28% → 20.68%) and a 5× improvement in binary AP (1.82% → 9.09%), at the cost of a 25 pp recall drop on BBBC041 (66.88% → 41.61%). The source-domain regression has a clear explanation: CLAHE's local contrast enhancement, tuned for cross-dataset color normalization, amplifies intra-image texture variation in BBBC041's already high-contrast Giemsa images. This creates spurious local maxima in the distance transform that `peak_local_max` interprets as seeds, fragmenting single cells into multiple sub-cell regions - each too small to achieve IoU ≥ 0.5 with the full GT box. The 10,764 v2 regions vs. 7,704 v1 regions (39% more), with recall dropping from 66.88% to 41.61%, is consistent with this over-segmentation hypothesis.

This result illustrates a domain-adaptation trade-off: a preprocessing step that normalizes the staining distribution gap between datasets improves cross-dataset performance while degrading source-domain metrics. Resolution of this trade-off requires either (i) dataset-adaptive CLAHE parameters (lower clip limit for BBBC041, higher for MP-IDB), or (ii) a learned stain normalization layer. Both are left to future work.

4.8. Dense Region Analysis

Stage 1 achieves 75.95% overall cell recovery on the test set. The 24% of cells not recovered can be attributed to two primary sources of error: (i) very pale, lightly-stained RBCs whose intensity distribution overlaps with the background, causing Otsu's global threshold to classify them as background; and (ii) dense clusters of 4–6 cells with no visible inter-cell gap, where the distance transform does not generate sufficient seed separation to split the cluster.

Table 11: Stage 1 ablation: v1 (Otsu + fixed parameters) vs. v2 (CLAHE + resolution-aware `peak_local_max`). Source domain = BBBC041 120-image test set; cross-dataset = MP-IDB 209-image set. All metrics at IoU ≥ 0.5. Binary AP includes only parasitic-stage classes.

	BBBC041 (source)		**MP-IDB (cross-dataset)**	
Metric	v1	v2	v1	v2
Watershed regions	7,704	10,764	4,726	52,222
Recall@IoU 0.5	66.88%	41.61%	1.28%	20.68%
Precision@IoU 0.5	51.36%	22.87%	0.38%	0.56%
F1@IoU 0.5	58.10%	29.52%	0.59%	1.09%
Binary Parasitized AP	29.10%	7.40%	1.82%	9.09%

The dense-region recall of 50.94% (over two qualifying test images with $\geq$ 100 GT boxes) indicates that cluster merging is the dominant failure mode in high-density images. This is consistent with the observation that our oversized-region filter removes 5–8% of Stage 1 regions per image in dense smears. A critical distinction from Baseline A is that Stage 1 errors are visible and spatially locatable - merged clusters are flagged in the output image - whereas NMS errors in Baseline A are silent suppressions with no visual indicator.

4.9. Explainability Analysis

4.9.1. Grad-CAM++ Visualizations

Figure 19 shows Stage 1 watershed output on a representative test image: correctly detected RBCs are outlined in red, detected parasites are highlighted with colored thick borders and class labels, and oversized merged regions are marked in gray.

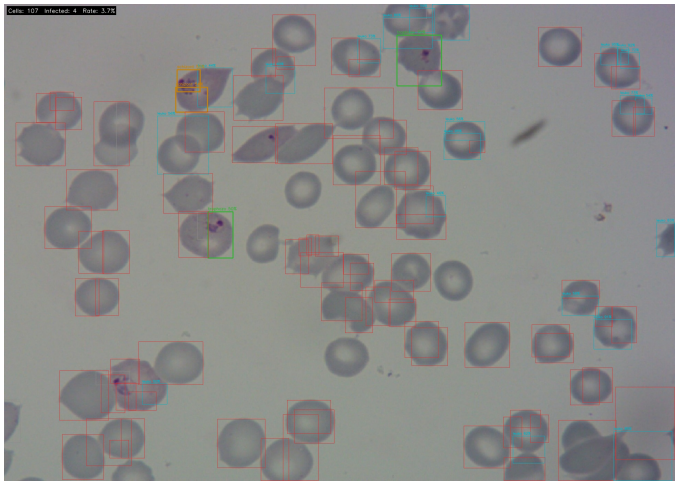


Figure 19: Stage 1 watershed output on a representative test image (64985a1e, 42 valid regions detected, 5 oversized merged clusters filtered). Red boxes: red blood cells. Green box: trophozoite (43% confidence). Cyan: leukocytes. Gray "merged?" labels: oversized regions excluded from Stage 2. The infection summary overlay (top left) shows 4 infected cells at 9.5% rate. Image courtesy NIH BBBC041.

Figure 20 shows the Grad-CAM++ gallery for the same image: each detected parasite is shown at 160×160 pixels with the heatmap overlaid in jet colormap.

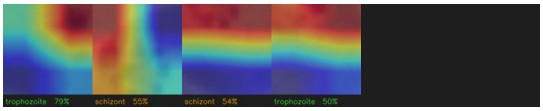


Figure 20: Grad-CAM++ crop gallery for the representative test image. Each panel shows a detected parasitic cell at 160×160 pixels with the heatmap overlaid (jet colormap, $\alpha = 0.5$). Red-yellow regions indicate pixels that most strongly contributed to the model's classification decision. Labels show class name and softmax confidence. Image courtesy NIH BBBC041.

Figure 21 shows the full-image Grad-CAM++ overlay. To interpret the figure: the heatmap uses a jet colormap where **red-yellow regions indicate pixels that most strongly influenced the model's classification decision**, and cool blue regions contributed minimally. The heatmap is projected only onto the bounding box regions of confirmed parasite detections; the remainder of the 1600×1200 smear is shown unchanged, providing clinical context. A clinician should read this view as a spatial audit trail: if the highlighted region aligns with the parasite body (e.g., the chromatin mass of a trophozoite or schizont), the model's decision is biologically plausible; if the heatmap falls on a staining artefact or cell boundary, the prediction warrants manual review.

The spatial heatmaps in Figures 20 and 21 consistently highlight the central or peripheral chromatin regions of the cell crop, consistent with parasite morphology in Giemsa-stained smears. For trophozoite and schizont predictions, the highest-activation region aligns with the dense chromatin mass. For ring-stage detections (not present in this particular image), the activation rim would be expected to follow the peripheral chromatin outline. This spatial specificity is the property that makes the output clinically auditable: a microscopist can immediately assess whether the model's salient region corresponds to a biologically meaningful structure or to a staining artefact.

4.9.2. Quantitative Localization Validation

The qualitative galleries above are illustrative but do not, by themselves, establish that Grad-CAM++ activation is concentrated on the cell rather than spread uniformly across the crop. We quantify this with an energy-in-box ratio: for each correctly classified parasite crop, the fraction

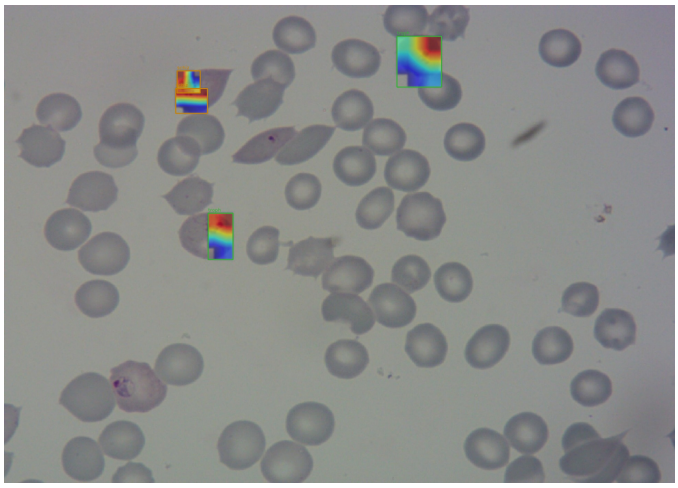


Figure 21: Full-image Grad-CAM++ overlay. The heatmap is spliced back onto the original 1600×1200 smear only at parasite-detected bounding box locations using a soft spatial mask (Gaussian-blurred boundary). The rest of the image is shown unchanged. Parasite bounding boxes are drawn in class color. Image courtesy NIH BBBC041.

of total heatmap activation energy falling inside the tight ground-truth box, compared against a chance baseline equal to the geometric fraction of the 64×64 crop occupied by that same box. A ratio indistinguishable from chance would indicate the heatmap conveys no localization information beyond the box's own size.

Evaluated at the layer conventionally used for EfficientNet-style backbones (`features[-1]`), this metric returned a null result: ratio 0.8343 vs. chance 0.8340 (difference +0.0003), statistically indistinguishable from the geometric baseline. Diagnosis: at 64×64 input resolution, `features[-1]` is downsampled to approximately 2×2 spatial positions – only four distinguishable regions, insufficient to separate "inside the box" from the crop's narrow margin once upsampled back to input resolution. Rather than report this null result as an inherent limitation of Grad-CAM++ on small crops, we ran a layer ablation over `features[2]`–`features[5]`, measuring each layer's true spatial resolution empirically via forward hooks and recomputing the same ratio-vs-chance metric with the already-trained classifier (no retraining). `features[5]` (4×4 resolution, one block deeper than the equally-sized `features[4]`) was the only candidate to beat chance by a non-trivial margin, indicating that both spatial resolution and layer depth (feature discriminativeness) jointly determine localization quality – resolution alone did not fully explain the pattern.

Adopting `features[5]` and re-evaluating with a paired significance test (paired t-test and Wilcoxon signed-rank test, since ratio and chance are computed on the same crop and are therefore correlated) gives: ratio 0.8831 vs. chance 0.8346 (+0.0485), paired $t(325) = 13.580$, $p = 1.40 \times 10^{-33}$; Wilcoxon $W = 7762.0$, $p = 1.39 \times 10^{-28}$ ($n = 326$ correctly-classified parasite crops across the four parasite classes, out of $n = 429$ evaluated). The effect holds individually for

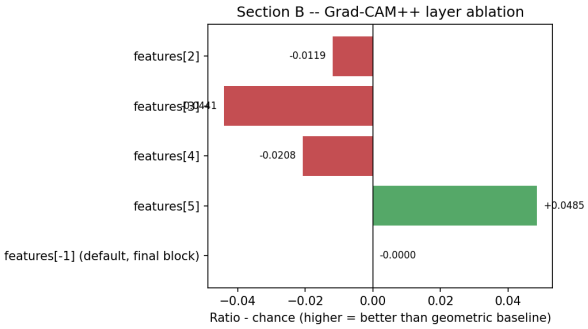


Figure 22: Grad-CAM++ target-layer ablation: energy-in-box ratio minus chance baseline for each candidate layer. `features[5]` is the only layer to beat chance by a non-trivial margin; the default `features[-1]` is statistically null (−0.0000).

every class: schizont +0.0791, gametocyte +0.0660, trophozoite +0.0472, ring +0.0334 (all $p < 0.003$). This confirms that Grad-CAM++ activation is concentrated on the annotated cell body significantly beyond what crop geometry alone would predict, turning the qualitative galleries of Figures 20–21 into a quantitatively validated claim.

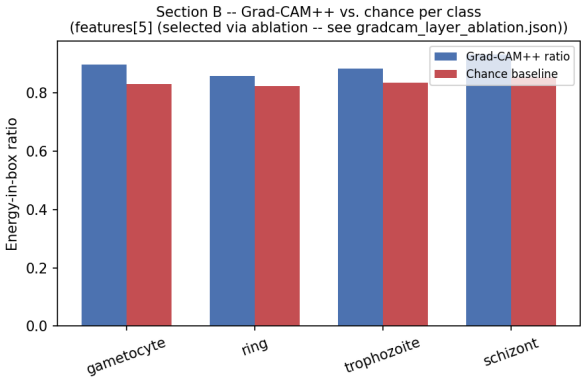


Figure 23: Grad-CAM++ energy-in-box ratio vs. chance baseline, per parasite class, at the finalized `features[5]` target layer. All four classes exceed their respective chance baseline.

4.10. Summary of Key Results

Table 12 consolidates all quantitative results from Sections 4.2.1–4.7 into a single reference. Metrics are grouped by evaluation domain (BBBC041 source domain; MP-IDB cross-dataset) and by pipeline component, enabling direct comparison across methods.

The table illustrates three key findings. First, the source-domain mAP gap between Baseline A (58.99%) and Pipeline B v1 (8.67%) reflects the structural difference between trained box regression (Faster R-CNN) and unsupervised watershed boundary extraction: Faster R-CNN proposals are explicitly optimized to match GT box geometry, while watershed regions are not. The binary parasitized AP of 29.10% may represent a more clinically relevant metric, capturing the pipeline's core task (flag any infected

Table 12: Consolidated results summary. Baseline A = Faster R-CNN; Baseline B = YOLOv8s (Section 3.4); Pipeline B = two-stage decoupled framework (Stage 1 watershed + Stage 2 EfficientNet-B0). Stage 1 v1 = Otsu + fixed distance threshold; Stage 1 v2 = CLAHE + resolution-aware `peak_local_max`. All detection metrics at IoU ≥ 0.5. † = cross-dataset zero-shot. N/A = not applicable; — = not evaluated.

Metric	**Baseline A**	**Baseline B**	**Pipeline B v1**	**Pipeline B v2**
BBBC041 - source domain (120 test images, 5,917 GT boxes)				
Stage 1 cell recovery (centroid)	N/A	N/A	75.95%	—
Stage 1 recall @ IoU 0.5	N/A	N/A	66.88%	41.61%
Stage 1 precision @ IoU 0.5	N/A	N/A	51.36%	22.87%
mAP@0.5 (all classes)	58.99%	71.24%	8.67%	0.78%
Binary Parasitized AP@0.5	—	—	29.10%	7.40%
Ring AP@0.5	57.17%	75.65%	8.22%	—
Trophozoite AP@0.5	67.22%	77.05%	8.27%	—
Schizont AP@0.5	24.57%	38.45%	13.64%	—
Gametocyte AP@0.5	25.95%	57.27%	4.55%	—
Stage 2 crop accuracy (val)	N/A	N/A	98.36%	98.36%
MP-IDB - cross-dataset† (209 images, 1,407 infected cells)				
Stage 1 recall @ IoU 0.5	N/A	N/A	1.28%	20.68%
Binary Parasitized AP@0.5	N/A	N/A	1.82%	9.09%
P. malariae recall	N/A	N/A	4.65%	86.0%
P. ovale recall	N/A	N/A	0.00%	60.6%
P. vivax recall	N/A	N/A	0.00%	32.8%
P. falciparum recall	N/A	N/A	1.26%	16.8%

cell)while reducing sensitivity to exact boundary alignment. Second, Baseline B (YOLOv8s) raises mAP@0.5 to 71.24%, confirming that a modern single-stage detector meaningfully outperforms the older two-stage architecture on this task – yet its rare-class AP (schizont 38.45%, gametocyte 57.27%) still trails Pipeline B's crop-level classification accuracy on the same classes (87.5%, 75.0%), indicating that the class-imbalance problem persists even under architectural modernization and is not solved by detector choice alone. Third, Stage 1 v2 demonstrates that the 1.28% MP-IDB recall failure of v1 was a contrast normalization problem: CLAHE preprocessing alone raises cross-dataset recall 16× (to 20.68%) and AP 5× (to 9.09%), without any retraining of Stage 2.

5. Discussion

5.1. Interpretation of Findings

Two results from Section 4 warrant careful interpretation before drawing broader conclusions. First, the 98.36% Stage 2 accuracy is a best-case measurement taken on crops extracted from perfect ground-truth boxes; it confirms classifier capability under ideal input conditions but does not reflect end-to-end pipeline recall, which is bounded by the 75.95% Stage 1 centroid recovery rate.

The more structurally significant finding is the Baseline A loss curve. Validation loss diverges from training loss at epoch 8 – before any conventional overfitting is possible – and subsequently *increases* after the learning rate step at epoch 50, a reduction that should improve generalization. This reproducible pattern is consistent with the closed-world detection paradigm applied to sparsely annotated data: the model is trained to suppress signal at unannotated cell locations, and every optimization step that reduces training loss deepens that suppression. This structural bias is not resolvable through additional training or regularization, and strongly motivates the architectural decision to decouple segmentation from classification.

The 75.95% Stage 1 cell recovery rate places an upper bound on the end-to-end pipeline performance: approximately one in four ground-truth cells is not recovered by watershed, and these cells cannot be classified by Stage 2. For the rare parasitic stages (schizont: 11 test instances, gametocyte: 12 test instances), a 75% recovery rate means approximately 8–9 instances reach the classifier. The practical consequence is that sensitivity for very rare parasites depends on the quality of Stage 1, and improving Stage 1 recovery is the highest-leverage direction for future work.

The per-class accuracy comparisons in Table 8 must be interpreted carefully. Crop accuracy and detection AP are not equivalent: AP penalizes false positives (spurious detections) in addition to missed detections, while accuracy is computed only on ground-truth crops. Nonetheless, the comparison is meaningful in the following sense: the Stage 2 classifier, when given a correctly segmented cell crop, produces substantially better rare-class performance than Baseline A achieves on the same classes end-to-end. This is consistent with the interpretation that the imbalance problem (and therefore Focal Loss) is a primary constraint for rare-class performance, not architectural capacity.

5.2. Clinical Relevance and Practical Implications

The combination of watershed-based universal cell recovery and Grad-CAM++ explainability produces a system

with two properties that matter for clinical adoption. First, the output is spatially auditable: a clinician can look at the heatmap and ask whether the model is attending to the parasite or to an unrelated feature. This auditability is absent from all existing whole-slide malaria detection systems. Second, the system fails visibly: merged cluster regions are explicitly flagged in the output rather than silently misclassified, allowing the operator to know where Stage 1 struggled. NMS-based detectors fail silently, with no visual indicator of suppressed detections.

EfficientNet-B0's 5.3M-parameter footprint and ∼2-second CPU inference time make the system deployable without GPU infrastructure, addressing a practical constraint in resource-limited settings. The full pipeline can be packaged as a web application requiring only an uploaded JPEG image and a CPU compute instance.

5.3. Limitations and Future Work

Stage 1 recovery ceiling. The 75.95% recovery rate reflects a known limitation of global Otsu thresholding: very pale, lightly-stained RBCs overlap in intensity distribution with the background and are not detected. Adaptive thresholding or multi-channel segmentation could potentially recover these cells, at the risk of increasing noise detections. This trade-off requires careful empirical evaluation.

Dense-region recall. The 50.94% dense-region recall is computed on only two qualifying test images, limiting statistical confidence. A dataset with more very-dense images would be needed for a robust evaluation of the watershed's dense-region performance.

End-to-end mAP and Stage 1 box precision. As reported in Section 4.4, the mAP gap between Pipeline B and Baseline A is attributable to Stage 1 watershed boundary precision rather than Stage 2 classification quality: watershed regions are organically shaped and are not trained to fit GT box boundaries, causing IoU@0.5 matching to fail for cells that are spatially detected but whose region boundary falls short of the 0.5 threshold. The binary parasitized AP@0.5 may therefore serve as a more clinically relevant summary metric than multi-class mAP for this pipeline architecture. Stage 1 v2 improvements (resolution-aware seeding, CLAHE preprocessing) are expected to narrow this gap by improving region boundary precision.

Single train/test split. All reported detection results (Baseline A, Baseline B, Pipeline B end-to-end) use a fixed 80/20 image-level split with random seed 42, applied identically to all three methods so they are compared on exactly the same held-out images. Cross-dataset evaluation on MP-IDB provides independent out-of-distribution evidence that is not sensitive to this particular split. For Stage 2 specifically, we additionally quantified split sensitivity directly: 5-fold stratified cross-validation gives 97.33% ± 0.49%, tightly consistent with the single-split 98.36% figure (Section 4.3). This does not extend to the detection-level comparisons against Baseline A/B, which remain single-split; k-fold evaluation of the full end-to-end pipeline is a natural extension of this work.

Learned segmentation baseline still trails on raw recall. Section 4.2.3 shows that even with watershed-style post-processing, the U-Net baseline's recall (62.89%) remains ∼4 points below Stage 1's raw-intensity watershed (66.88%), despite substantially higher precision and F1. The synthetic ellipse-mask training target (a proxy for the true cell boundary, since BBBC041 provides no pixel-level masks) is a plausible contributor, and a larger U-Net or one trained at native 1600×1200 resolution rather than 512×384 may close the remaining gap; we did not explore either due to the compute budget available for this revision.

Dataset scope and cross-dataset generalization. Both BBBC041 and MP-IDB use Giemsa thin-smear staining. Thick smear microscopy – the preferred technique for *P. vivax* and low-parasitaemia infections – presents a fundamentally different visual appearance (lysed cells, complex background) and requires a dedicated evaluation before clinical deployment can be considered in those settings. More broadly, Section 3.1.2 introduces MP-IDB as a held-out cross-validation set, but no parameter re-tuning was performed, and the 11.3× reduction in relative cell prominence is expected to reduce Stage 1 recall. Resolution-aware Stage 1 parameter adaptation is the most tractable immediate remedy.

6. Conclusion

We have presented MalariAI, a two-stage decoupled framework for automated malaria cell detection and stage classification from Giemsa-stained thin blood smears. The framework addresses three structural failure modes that collectively prevent existing end-to-end detectors from being clinically deployable: annotation incompleteness (P1), NMS suppression in dense regions (P2), and opaque black-box outputs (P3).

Stage 1 applies a distance-transform guided watershed algorithm with no annotation input, recovering 75.95% of all ground-truth cells in the NIH BBBC041 120-image test set. Stage 2 applies a focal-loss-trained EfficientNet-B0 classifier on 64×64 crops extracted by Stage 1, achieving 98.36% validation accuracy on the full 7-class problem. The rare-class performance improvement over both detection baselines is substantial: schizont accuracy rises from 24.57% AP (Baseline A, Faster R-CNN) and 38.45% AP (Baseline B, YOLOv8s) to 87.5% per-class accuracy; gametocyte from 25.95% and 57.27% AP, respectively, to 75.0%. The comparison against Baseline B confirms this gap is not merely an artefact of an outdated detection architecture: a current-generation single-stage detector narrows it but does not close it. Grad-CAM++ spatial heatmaps are produced for every detected cell, enabling per-cell spatial audit trails that are absent from all prior whole-slide detection systems; a quantitative energy-in-box analysis confirms this activation is concentrated on the annotated cell body significantly

above chance (+0.0485, paired $p = 1.4 \times 10^{-33}$), rather than resting on qualitative inspection alone.

We additionally benchmarked Stage 1's annotation-free watershed against a conventionally-trained U-Net segmentation baseline on the identical 120-image test set. Naive thresholding of the U-Net's predicted mask underperforms watershed substantially (25.28% vs. 66.88% recall), reproducing the same touching-cell merging problem that motivates watershed splitting in Stage 1. Applying that same watershed-splitting technique to the U-Net's probability map instead of raw pixel intensity closes most of the recall gap (62.89%) while exceeding Stage 1 on precision (83.28% vs. 51.36%) and F1 (0.717 vs. 0.581) – indicating that the post-processing strategy, not the choice between a learned or unsupervised signal source, is the primary determinant of detection quality in this task.

The cross-dataset characterization of MP-IDB more accurately reflects the difficulty of generalisation across datasets: infected cells in MP-IDB cover 11.3× less of the image frame than in BBBC041, directly predicting reduced Stage 1 recall without parameter re-tuning. This finding motivates the primary next step: resolution-aware Stage 1 adaptive thresholding.

End-to-end evaluation confirms that Pipeline B achieves a binary parasitized AP@0.5 of 29.10% on BBBC041 (Stage 1 v1). On MP-IDB, Stage 1 v2 (CLAHE + resolution-aware `peak_local_max`) raises recall from 1.28% to 20.68% and binary AP from 1.82% to 9.09%, supporting the scale-gap hypothesis and suggesting that the failure mode is consistent with a contrast-normalization mismatch rather than an architectural limitation. The ablation (Table 11) reveals a domain-adaptation trade-off: v2 improves cross-dataset performance by 5× but reduces source-domain binary AP from 29.10% to 7.40%, motivating dataset-adaptive CLAHE parameters as the primary future direction. Beyond Stage 1 improvements, two further directions are prioritized. First, evaluation on thick blood smear datasets is required before the pipeline can be considered for *P. vivax* or low-parasitaemia settings, where the visual appearance differs fundamentally from the Giemsa thin smears used here. Second, 5-fold stratified cross-validation on Stage 2 crops confirms the single-split accuracy estimate is stable (97.33% ± 0.49% vs. 98.36%), aligning with the evaluation protocol used in published benchmarks such as [13] and [14]; extending this variance analysis to the full end-to-end detection pipeline (rather than Stage 2 crops alone) remains a natural next step.

Author Contributions

K.A. Apurba: Conceptualization, methodology, software (web application), formal analysis, writing: original draft, visualization. **M.H. Hasan:** System diagram, design, software, writing: review and editing. **M. Ali:** Conceptualization (Grad-CAM++ integration), writing: review and editing. **T. Rahman:** Supervision, writing: review and editing.

Acknowledgements

The authors gratefully acknowledge Prof. Amr Abdel-Dayem (Laurentian University, Canada) for guidance during the Image Processing and Computer Vision course within the M.Sc. program in Computational Sciences (Fall 2023).

Code and Demo Availability

The full codebase, trained model checkpoints, evaluation scripts, and reproduction instructions are publicly available at:

- **GitHub repository:** https://github.com/Anaskaysar/MalariAI
- **Interactive demo (HuggingFace Space):** https://huggingface.co/spaces/Kaysarulanas/MalariAI

The demo accepts any Giemsa-stained blood smear image and returns the annotated smear, per-class cell counts, infection rate, and Grad-CAM++ heatmaps without requiring local installation.

Ethics Statement

This study did not involve the collection of new data from human participants or animal subjects by the authors. All experiments were conducted exclusively on two previously published, publicly available, and fully de-identified benchmark datasets: NIH BBBC041 [44] and MP-IDB [46]. Neither dataset contains personally identifiable patient information, and both are released for open research use by their original providers. As no new human or animal data were collected, institutional ethical approval was not required for this study.

Declaration of Competing Interests

The authors declare that they have no known competing financial interests or personal relationships that could have appeared to influence the work reported in this paper.

Funding

This research did not receive any specific grant from funding agencies in the public, commercial, or not-for-profit sectors.

Declaration of Generative AI and AI-Assisted Technologies in the Writing Process

During the preparation of this work, the authors used Claude (Anthropic) to assist with grammar checking, sentence restructuring, and consistency review of the manuscript text. After using this tool, the authors reviewed and edited the content as needed and take full responsibility for the content of the published article.

References

[1] World Health Organization, World malaria report 2023, Tech. rep., WHO Press, Geneva (2023). URL https://www.who.int/teams/global-malaria-programme/reports/world-malaria-report-2023

[2] P. J. Delves, S. J. Martin, D. R. Burton, I. M. Roitt, Roitt's Essential Immunology, 13th Edition, Wiley-Blackwell, 2017.

[3] M. Poostchi, K. Silamut, R. J. Maude, S. Jaeger, G. Thoma, Image analysis and machine learning for detecting malaria, Translational Research 194 (2018) 36–55. doi:10.1016/j.trsl.2017.12.004.

[4] S. Rajaraman, S. K. Antani, M. Poostchi, K. Silamut, M. A. Hossain, R. J. Maude, S. Jaeger, G. R. Thoma, Pre-trained convolutional neural networks as feature extractors toward improved malaria parasite detection in thin blood smear images, PeerJ 6 (2018) e4568. doi:10.7717/peerj.4568.

[5] R. Singh, C. Prabha, S. Abdulla, Optimized CNN framework for malaria detection using Otsu thresholding-based image segmentation, Scientific Reports 15 (2025) 40117. doi:10.1038/s41598-025-23961-5.

[6] S. Ren, K. He, R. Girshick, J. Sun, Faster R-CNN: Towards real-time object detection with region proposal networks, in: Advances in Neural Information Processing Systems (NeurIPS), 2015, pp. 91–99. URL https://arxiv.org/abs/1506.01497

[7] D. Sukumarran, K. Hasikin, A. S. M. Khairuddin, R. Ngui, W. Y. Wan Sulaiman, I. Vythilingam, P. C. S. Divis, An optimised YOLOv4 deep learning model for efficient malarial cell detection in thin blood smear images, Parasites & Vectors 17 (2024) 188. doi:10.1186/s13071-024-06215-7.

[8] R. Parveen, B. Qui, W. Song, N. Al-Kahtani, M. M. Jamjoom, S. M. Mostafa, N. Sultan, J. Fatima, Trustworthy deep learning for malaria diagnosis using explainable artificial intelligence, Scientific Reports 15 (2025) 45037. doi:10.1038/s41598-025-28387-7.

[9] M. R. Islam, M. Nahiduzzaman, M. O. F. Goni, A. Sayeed, M. S. Anower, M. Ahsan, J. Haider, Explainable transformer-based deep learning model for the detection of malaria parasites from blood cell images, Sensors 22 (12) (2022) 4358. doi:10.3390/s22124358.

[10] O. O. Awe, P. N. Mwangi, S. K. Goudoungou, R. V. Esho, O. S. Oyejide, Explainable AI for enhanced accuracy in malaria diagnosis using ensemble machine learning models, BMC Medical Informatics and Decision Making 25 (2025) 152. doi:10.1186/s12911-025-02874-3.

[11] R. R. Selvaraju, M. Cogswell, A. Das, R. Vedantam, D. Parikh, D. Batra, Grad-CAM: Visual explanations from deep networks via gradient-based localization, in: IEEE International Conference on Computer Vision (ICCV), 2017, pp. 618–626. URL https://arxiv.org/abs/1610.02391

[12] A. Chattopadhyay, A. Sarkar, P. Howlader, V. N. Balasubramanian, Grad-CAM++: Generalized gradient-based visual explanations for deep convolutional networks, in: IEEE Winter Conference on Applications of Computer Vision (WACV), 2018, pp. 839–847. URL https://arxiv.org/abs/1710.11063

[13] M. Mujahid, F. Rustam, R. Shafique, E. Caro Montero, E. Silva Alvarado, I. de la Torre Diez, I. Ashraf, Efficient deep learning-based approach for malaria detection using red blood cell smears, Scientific Reports 14 (2024) 13249. doi:10.1038/s41598-024-63831-0.

[14] O. P. Mmileng, A. Whata, M. Olusanya, S. Mhlongo, Application of ConvNeXt with transfer learning and data augmentation for malaria parasite detection in resource-limited settings using microscopic images, PLOS One 20 (6) (2025) e0313734. doi:10.1371/journal.pone.0313734.

[15] O. O. Oladimeji, A. O. Ibitoye, A novel attention-enhanced hybrid deep learning approach for malaria diagnosis in microscopic cell images, Informatics and Health 3 (2026) 41–47. doi:10.1016/j.infoh.2025.11.004.

[16] A. Gaouar, S. H. Cherif, A. Rahmoun, M. El Habib Daho, Explainable AI for early malaria detection using stacked-LSTM and attention mechanisms, Informatics in Medicine Unlocked 57 (2025) 101667. doi:10.1016/j.imu.2025.101667.

[17] A. T. Issah, I. Seidu, C. Mukamakuza, Detection versus instance segmentation for multi-species malaria diagnosis: A head-to-head comparison and multi-dataset validation of YOLOv12 architectures with small object optimization, in: Proceedings of Machine Learning Research, Vol. 315, 2026, pp. 4683–4702. URL https://proceedings.mlr.press/v315/issah26a.html

[18] D. Sukumarran, K. Hasikin, A. S. M. Khairuddin, R. Ngui, W. Y. W. Sulaiman, I. Vythilingam, P. C. S. Divis, Machine and deep learning methods in identifying malaria through microscopic blood smear: A systematic review, Engineering Applications of Artificial Intelligence 133 (2024) 108529. doi:10.1016/j.engappai.2024.108529.

[19] D. R. Loh, W. X. Yong, J. Yapeter, K. Subburaj, R. Chandramohanadas, A deep learning approach to the screening of malaria infection: Automated

and rapid cell counting, object detection and instance segmentation using Mask R-CNN, Computerized Medical Imaging and Graphics 88 (2021) 101845. doi:10.1016/j.compmedimag.2020.101845.

[20] M. Delgado-Ortet, A. Molina, S. Alférez, J. Rodellar, A. Merino, A deep learning approach for segmentation of red blood cell images and malaria detection, Entropy 22 (6) (2020) 657. doi:10.3390/e22060657.

[21] A. Pandiaraj, P. R. Kshirsagar, R. Thiagarajan, T. K. Tak, B. Sivaneasan, A robust malaria cell detection framework using adaptive and atrous convolution-based recurrent MobileNetV2 with Trans-MobileUNet^{++}-based abnormality segmentation, Journal of Imaging Informatics in Medicine 38 (2025) 2381–2411. doi:10.1007/s10278-024-01311-7.

[22] M. Marks, U. Israel, R. Dilip, Q. Li, C. Yu, E. Laubscher, A. Iqbal, E. Pradhan, A. Ates, M. Abt, C. Brown, E. Pao, S. Li, A. Pearson-Goulart, P. Perona, G. Gkioxari, R. Barnowski, Y. Yue, D. Van Valen, CellSAM: a foundation model for cell segmentation, Nature Methods 22 (2025) 2585–2593. doi:10.1038/s41592-025-02879-w.

[23] R. Sun, Y. Yang, K. Guo, C. Jiang, D. Xu, Z. Liu, T. Pan, L. Han, X. Jiang, W. Wei, Y. Cheng, Disco: Densely-overlapping cell instance segmentation via adjacency-aware collaborative coloring, in: International Conference on Learning Representations (ICLR), 2026.

[24] N. Otsu, A threshold selection method from gray-level histograms, IEEE Transactions on Systems, Man, and Cybernetics 9 (1) (1979) 62–66. doi:10.1109/TSMC.1979.4310076.

[25] S. Beucher, F. Meyer, The morphological approach to segmentation: the watershed transformation, in: E. Dougherty (Ed.), Mathematical Morphology in Image Processing, Marcel Dekker, New York, 1992, pp. 433–481.

[26] C. V. Angkoso, Y. F. Hendrawan, A. Kusumaningsih, A. Bauravindah, R. T. Wahyuningrum, D. A. Dewi, Research on different automatic segmentation methods for color cascading framework in detecting malaria infection, Array 29 (2026) 100658. doi:10.1016/j.array.2025.100658.

[27] K. He, X. Zhang, S. Ren, J. Sun, Deep residual learning for image recognition, in: IEEE/CVF Conference on Computer Vision and Pattern Recognition (CVPR), 2016, pp. 770–778. doi:10.1109/CVPR.2016.90.

[28] T.-Y. Lin, P. Dollár, R. Girshick, K. He, B. Hariharan, S. Belongie, Feature pyramid networks for object detection, in: IEEE/CVF Conference on Computer Vision and Pattern Recognition (CVPR), 2017, pp. 2117–2125. doi:10.1109/CVPR.2017.106.

[29] J. Hung, A. Carpenter, Applying faster R-CNN for object detection on malaria images, in: Proceedings of the IEEE/CVF Conference on Computer Vision and Pattern Recognition Workshops (CVPRW), 2017. doi:10.1109/CVPRW.2017.112.

[30] G. Jocher, A. Chaurasia, J. Qiu, Ultralytics YOLOv8, https://github.com/ultralytics/ultralytics (2023).

[31] K. He, G. Gkioxari, P. Dollár, R. Girshick, Mask R-CNN, in: IEEE International Conference on Computer Vision (ICCV), 2017, pp. 2961–2969.
URL https://arxiv.org/abs/1703.06870

[32] F. Li, H. Zhang, S. Liu, J. Guo, L. M. Ni, L. Zhang, DN-DETR: Accelerate DETR training by introducing query denoising, in: IEEE/CVF Conference on Computer Vision and Pattern Recognition (CVPR), 2022, pp. 13619–13629.
URL https://arxiv.org/abs/2203.01305

[33] E. Guemas, B. Routier, T. Ghelfenstein-Ferreira, C. Cordier, S. Hartuis, B. Marion, S. Bertout, E. Varlet-Marie, D. Costa, G. Pasquier, Automatic patient-level recognition of four *Plasmodium* species on thin blood smear by a real-time detection transformer (RT-DETR) object detection algorithm: a proof-of-concept and evaluation, Microbiology Spectrum 12 (2) (2024) e01440–23. doi:10.1128/spectrum.01440-23.

[34] X. Bai, B. Ma, C. Li, Y. Xia, Tackling the incomplete annotation issue in universal lesion detection task by exploratory training, IEEE Transactions on Medical Imaging (2023). doi:10.1109/TMI.2023.3321488.

[35] A. Kirillov, E. Mintun, N. Ravi, H. Mao, C. Rolland, L. Gustafson, T. Xiao, S. Whitehead, A. C. Berg, W.-Y. Lo, P. Dollár, R. Girshick, Segment anything, in: IEEE/CVF International Conference on Computer Vision (ICCV), 2023, pp. 4015–4026.
URL https://arxiv.org/abs/2304.02643

[36] O. Ronneberger, P. Fischer, T. Brox, U-Net: Convolutional networks for biomedical image segmentation, in: Medical Image Computing and Computer-Assisted Intervention (MICCAI), Vol. 9351 of Lecture Notes in Computer Science, 2015, pp. 234–241. doi:10.1007/978-3-319-24574-4_28.

[37] V. Badrinarayanan, A. Kendall, R. Cipolla, SegNet: A deep convolutional encoder-decoder architecture for image segmentation, IEEE Transactions on Pattern Analysis and Machine Intelligence 39 (12) (2017) 2481–2495. doi:10.1109/TPAMI.2016.2644615.

[38] Z. Zhou, M. M. R. Siddiquee, N. Tajbakhsh, J. Liang, UNet++: A nested U-Net architecture for medical image segmentation, in: Deep Learning in Medical

Image Analysis and Multimodal Learning for Clinical Decision Support (MICCAI Workshop), 2018, pp. 3–11.
URL https://arxiv.org/abs/1807.10165

[39] F. Horst, T. Rempe, J. Li, C. Brockmann, T. Lawitzki, S. Amirpour, G. Baldini, C. Ulrich, S. Denner, J. Kleesiek, CellViT: Vision transformers for precise cell segmentation and classification, Medical Image Analysis 94 (2024) 103143. doi:10.1016/j.media.2024.103143.

[40] V. Petsiuk, R. Jain, V. Manjunatha, V. I. Morariu, A. Mehra, V. Ordonez, K. Saenko, Black-box explanation of object detectors via saliency maps, in: IEEE/CVF Conference on Computer Vision and Pattern Recognition (CVPR), 2021, pp. 11443–11452.
URL https://arxiv.org/abs/2006.03204

[41] Y. Zheng, E. Abila, E. Chrenková, I. Buljan, J. Winkler, A. F. Rendeiro, LazySlide: accessible and interoperable whole-slide image analysis, Nature Methods 23 (2026) 728–731. doi:10.1038/s41592-026-03044-7.

[42] H. Guan, M. Liu, Domain adaptation for medical image analysis: A survey, IEEE Transactions on Biomedical Engineering 69 (3) (2022) 1173–1185. doi:10.1109/TBME.2021.3117407.

[43] R. Nakasi, J. N. Nabende, J. F. Tusubira, A. L. Bamundaga, A. Andama, A dataset of blood slide images for AI-based diagnosis of malaria, Data in Brief 58 (2025) 111190. doi:10.1016/j.dib.2024.111190.

[44] V. Ljosa, K. L. Sokolnicki, A. E. Carpenter, Annotated high-throughput microscopy image sets for validation, Nature Methods 9 (7) (2012) 637, dataset: https://bbbc.broadinstitute.org/BBBC041. doi:10.1038/nmeth.2083.

[45] T.-Y. Lin, P. Goyal, R. Girshick, K. He, P. Dollár, Focal loss for dense object detection, in: IEEE International Conference on Computer Vision (ICCV), 2017, pp. 2980–2988.
URL https://arxiv.org/abs/1708.02002

[46] A. Loddo, C. Di Ruberto, M. Kocher, G. Prod'Hom, MP-IDB: The malaria parasite image database for image processing and analysis, in: Processing and Analysis of Biomedical Information (SaMBa 2018), Vol. 11379 of Lecture Notes in Computer Science, 2019, pp. 57–65. doi:10.1007/978-3-030-13835-6_7.

[47] M. Tan, Q. V. Le, EfficientNet: Rethinking model scaling for convolutional neural networks, in: Proceedings of the International Conference on Machine Learning (ICML), 2019, pp. 6105–6114.
URL https://arxiv.org/abs/1905.11946

[48] J. Deng, W. Dong, R. Socher, L.-J. Li, K. Li, L. Fei-Fei, ImageNet: A large-scale hierarchical image database, in: IEEE/CVF Conference on Computer Vision and Pattern Recognition (CVPR), 2009, pp. 248–255. doi:10.1109/CVPR.2009.5206848.

[49] M. Yeung, E. Sala, C.-B. Schönlieb, L. Rundo, Unified focal loss: Generalising Dice and cross entropy-based losses to handle class imbalanced medical image segmentation, Computerized Medical Imaging and Graphics 95 (2022) 102026. doi:10.1016/j.compmedimag.2021.102026.

[50] B. H. M. van der Velden, H. J. Kuijf, K. G. A. Gilhuijs, M. A. Viergever, Explainable artificial intelligence (XAI) in deep learning-based medical image analysis, Medical Image Analysis 79 (2022) 102470. doi:10.1016/j.media.2022.102470.

[51] S. van der Walt, J. L. Schönberger, J. Nunez-Iglesias, F. Boulogne, J. D. Warner, N. Yager, E. Gouillart, T. Yu, the scikit-image contributors, scikit-image: image processing in Python, PeerJ 2 (2014) e453. doi:10.7717/peerj.453.

[52] T.-Y. Lin, M. Maire, S. Belongie, J. Hays, P. Perona, D. Ramanan, P. Dollár, C. L. Zitnick, Microsoft COCO: Common objects in context, in: European Conference on Computer Vision (ECCV), Vol. 8693 of Lecture Notes in Computer Science, 2014, pp. 740–755. doi:10.1007/978-3-319-10602-1_48.

Data Availability

The NIH BBBC041 dataset used in this study is publicly available at https://bbbc.broadinstitute.org/BBBC041. The MP-IDB cross-dataset validation set is publicly available at http://www.neuroimaging.it/malaria_parasite_image_database. The full codebase, trained model checkpoints, evaluation scripts, and reproduction instructions are available at https://github.com/Anaskaysar/MalariAI.